

# FlatLands: Generative Floormap Completion From a Single Egocentric View

Subhransu S. Bhattacharjee<sup>✉\*</sup>, Dylan Campbell<sup>✉</sup>, and Rahul Shome<sup>✉</sup>

School of Computing, The Australian National University, Canberra, Australia

**Abstract.** A single egocentric image typically captures only a small portion of the floor, yet a complete metric traversability map of the surroundings would better serve applications such as indoor navigation. We introduce FlatLands, a dataset and benchmark for single-view bird’s-eye view (BEV) floor completion. The dataset contains 270,575 observations from 17,656 real metric indoor scenes drawn from six existing datasets, with aligned observation, visibility, validity, and ground-truth BEV maps, and the benchmark includes both in- and out-of-distribution evaluation protocols. We compare training-free approaches, deterministic models, ensembles, and stochastic generative models. Finally, we instantiate the task as an end-to-end monocular RGB-to-floormaps pipeline. FlatLands provides a rigorous testbed for uncertainty-aware indoor mapping and generative completion for embodied navigation.

**Keywords:** scene completion · embodied AI · generative modeling

## 1 Introduction

Partial observability is a defining constraint in indoor autonomy — decisions must be made from sensory evidence that is incomplete, noisy, and inherently viewpoint-limited [2, 5, 35, 61, 104]. This paper targets a specific perception task that sits on this critical path — *inferring a usable traversability map from limited observations*. Robotic perception distills high-dimensional sensor streams into compact world models for mapping and planning under uncertainty [19, 45, 68, 69], combining geometric representations [65, 90, 100] with probabilistic occupancy estimates [41, 97, 144] and converting them into spatial abstractions such as metric-topological [10, 88, 141, 143] and semantic maps [67, 107, 118].

In contrast, we focus on a ground-plane bird’s-eye-view (BEV) floormap: a compact 2D grid of traversability obtained by projecting 3D geometry to the floor plane. BEV representations are widely adopted [73, 166] and directly support collision checking and reachability under uncertainty [85], making them an efficient abstraction for navigation tasks. Operational map-based reasoning from egocentric imagery has also shown strong practical value for localization and decision making [120]. Among sensing modalities, single-frame egocentric RGB is especially challenging [72, 105, 161]: one view observes a narrow frustum

\* Corresponding author: Subhransu.Bhattacharjee@anu.edu.au.

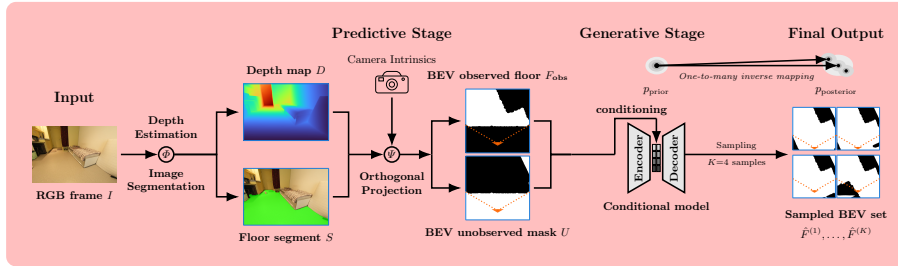


**Fig. 1:** Pipeline. From a single RGB image, our model predicts depth and floor segmentation and projects them to BEV, producing observed floor  $F_{\text{obs}}$  and unobserved mask  $U$ . A conditional generator then predicts floormap completions in the unobserved region, while preserving observed evidence.

while most traversable floor is unobserved due to occlusions. BEV completion from a single image is therefore inherently ambiguous and belongs to the class of Bayesian inverse problems [133, 138], where posterior reasoning is required rather than a single point estimate [33, 156]. Solving the single-frame case provides a per-step prior that can be fused temporally in multi-step navigation [4, 51, 110].

We study *single-view BEV floormap completion*: given one RGB image, infer a *distribution* over plausible traversability maps in the unobserved BEV while *exactly reproducing observed labels*. Since downstream decisions depend on uncertainty, we evaluate multi-hypothesis predictions using both fidelity and diversity metrics [46]. Indoor layouts exhibit strong structural regularities (rooms, doors, corridors), which are often modeled via grammar and pattern-theoretic priors [67, 94, 108]. Modern generative models can internalize these regularities for posterior inference and sampling [52, 76], and are increasingly exploited in robotics under uncertainty [12, 20, 21, 42, 113, 124]. Yet no standardized real-world benchmark exists for indoor BEV *metric* floormap completion.

To this end, we introduce FlatLands, a dataset with 17,656 real indoor scenes from six sources [7, 24, 34, 36, 147, 160]. Training data is synthesized from physically feasible camera centers and yaw headings, with visibility computed by field-of-view checks and ray-based occlusion as shown in Fig. 2b. After automatic curation, the dataset contains 270,575 observations with aligned floor evidence, visibility, validity, and ground-truth BEV maps. Evaluation uses the full test split with explicit in-distribution (ID) and out-of-distribution (OOD) partitioning, with ScanNet++ reserved strictly for test-only OOD evaluation and never used in training or validation. The task is also instantiated as a full monocular RGB-to-floormaps pipeline (Fig. 6). Quantitative evaluation uses standardized BEV-conditioned inputs, isolating completion quality from front-end estimation; end-to-end results confirm that method ranking transfers to realistic egocentric input. We benchmark training-free, deterministic, ensemble, and stochastic baselines under a shared protocol (Secs. 5 and 5.2).

*Contributions.* Our main contributions are as follows:

1. We formalize the single-view indoor BEV floor completion task and release *FlatLands*, the first benchmark of its kind with 270,575 observations from 17,656 real metric scenes across six datasets of RGB images and BEV floormaps, each with visibility masks, validity regions where the dataset has a floor or non-floor label, and full provenance metadata.
2. We design an extensive evaluation suite covering masked multi-hypothesis calibration and a monocular end-to-end RGB-to-floormaps pipeline that demonstrates real-sensor viability.
3. We report the performance of eleven methods spanning training-free approaches, deterministic predictors, epistemic ensembles, and three families of stochastic generators under a common conditioning input. We find that generative models better capture the observation-conditioned completion uncertainty than point estimates, and they also achieve stronger overall performance. A boundary-variance decomposition further reveals that epistemic ensembles conflate seed divergence with layout ambiguity, while conditional flow models localize uncertainty to structurally ambiguous regions.

## 2 Background and Related Work

*Indoor map completion and occupancy anticipation.* Classical occupancy mapping maintains per-cell Bayesian beliefs over traversability from sequential observations [40, 41, 57, 96, 144], while variable-resolution occupancy formulations improve representation efficiency in large spaces [97].

Under multi-step exploration, OccAnt [110] trains a CNN anticipator on Habitat simulations to project observed evidence into a predicted occupancy map; Katyal *et al.* [64] and Katsumata *et al.* [63] exploit temporal sequences for spatial anticipation. Aydemir *et al.* [3] use relational priors over object co-occurrence to complete partially observed rooms. Methods such as FloorNet [78], FloorSP [25], and room-layout estimation from monocular imagery [92] aim to reconstruct architectural plans from RGB-D, panoramic scans, or single-image cues with richer supervision. MapEx [51] and PIPE [4], which use the LaMa inpainting network [135], target multi-modal uncertainty under scoring with multi-step observations, while [113] applies diffusion priors to 3D occupancy completion. In navigation, the robot primarily needs a *traversability* map to denote where it can safely navigate [12, 41, 98].

*Image inpainting and outpainting via generative models.* Classical inpainting methods propagate structure into missing regions via PDE-based diffusion and exemplar matching [11, 23, 139]. Modern approaches are predominantly learned *e.g.* LaMa [135] couples large receptive fields (Fourier convolutions [31]) with adversarial training, while partial convolutions [79] build on the U-Net backbone [117] by masking convolutional updates. Related ideas also appear beyond natural images, including occupancy inpainting for 2D grid maps [150]. Outpainting (image extrapolation) extends content *beyond* observed boundaries and is typically less constrained than interior-hole inpainting, since boundary conditions are available only along the crop edge [149, 159]. Recent learned outpainting

methods explicitly target this regime, emphasizing semantic consistency and diversity [30, 71].

A complementary line of work treats in and outpainting as *conditional generation* under missing evidence. Context encoders [99] introduced learned context completion, while diffusion-based inpainting methods such as RePaint [86] and broader pixel-space diffusion models [52, 55, 95, 131] enforce conditioning via per-step masking. This masked-conditioning interface has since become standard in large-scale generators that support inpainting and outpainting [15, 101, 106, 112, 116]. For explicitly multi-modal completions, posterior-sampling mechanisms such as Probabilistic U-Net [66], hierarchical probabilistic inpainting [109], and conditional flow matching or rectified flows [76, 81, 145] provide principled ways to sample diverse outputs consistent with the observation. Here, by computing an observed BEV floormap, the binary BEV floormap completion task is effectively an *outpainting* problem on *binary metric grid maps* rather than RGB texture synthesis.

*BEV scene understanding by posterior sampling.* Autonomous driving BEV models [73, 103] couple geometric lifting with semantic prediction in synchronized multi-camera settings. Geometry-aware multi-view attention further improves transformer designs [91]. Neural map priors [155] and generative map layout estimation [165] extend this by incorporating learned spatial priors. Map-grounded visual localization methods such as OrienterNet [120] further show that operational image-to-map alignment is feasible at scale. Indoor BEV work is comparatively sparse: under a single egocentric view, occlusion and limited field of view leave large floor regions unobserved, making completion a partial-observability problem [2, 5, 19, 68]. Closest in spirit to our work, DiffBEV [166] and MapPrior [165] apply conditional diffusion to BEV completion and map layout estimation, but focus on outdoor driving with multi-view camera rigs. In contrast, we instantiate the inpainting and posterior-sampling paradigms for *indoor* BEV floor completion, where the target is a *binary* geometric map that respects metric floor structure—without expending capacity on RGB textures or dense semantic labels.

A partial BEV observation typically admits multiple plausible completions [4, 44, 51, 66]. The goal is to sample from  $p(F^* | F_{\text{obs}}, U)$  rather than collapse to a point estimate [133, 138]. Deterministic predictors target a single mode, whereas stochastic generators represent multimodal uncertainty that is relevant to safety-critical navigation [13, 35, 68].

*Inference efficiency.* A large body of work targets dense 3D reconstruction [122, 129, 137], including diffusion-based inverse solvers, image and text to mesh and single image novel view synthesis models [22, 54, 80, 82, 93, 113, 119, 130, 140]. These methods are complementary: they optimize 3D geometry or appearance for reconstruction and generation, typically producing volumetric occupancy grids, meshes, or radiance fields with non-trivial inference costs. In contrast, many navigation pipelines use a lightweight 2D occupancy or traversability grid aligned with motion feasibility (typically 2D), with lower storage requirements than

volumetric maps [132, 142], motivating our use of BEV representation in indoor scenes.

### 3 Problem and Framework

A *floormap* is a binary bird’s-eye-view (BEV) map encoding local traversability within a bounded indoor region. Binary traversability is the minimal spatial primitive consumed by collision-checking and path-planning modules [41, 85]; richer semantic labels are complementary but orthogonal to the completion task studied here. Given a single egocentric RGB image (Fig. 1), the goal is to predict the complete floormap—including unobserved portions that lie outside the camera frustum. We decouple this into two stages: *perception* of the observed floormap from the image, followed by *completion* of the unobserved portion.

#### 3.1 Task: Unobserved Floormap Completion

Let  $R$  denote a 2D bounded region of interest, situated relative to an oriented camera pose. Without loss of generality,  $R$  is discretized as an  $H \times W$  grid at a fixed metric resolution  $\Delta$  (m/px). Given an RGB image  $I$ , the camera’s field-of-view partitions  $R$  into an *observed* sub-region  $R_O \subseteq R$  and its complement, the *unobserved* region  $R_U = R \setminus R_O$ . The observed floormap  $F_{\text{obs}}$  is a binary map over  $R_O$  that records per-cell traversability,  $F_{\text{obs}}(x) = \mathbb{1}(x \text{ is traversable})$  for each  $x \in R_O$ . In practice,  $F_{\text{obs}}$  is estimated from  $I$  via the perception front-end described in Sec. 3.2.

The unobserved floormap  $F_{\text{uno}}$ , defined analogously over  $R_U$ . Since a single partial observation does not generally determine  $F_{\text{uno}}$  uniquely, we cast the task as sampling from the posterior  $P(F_{\text{uno}} | I)$  as a conditional inverse problem [133]. A parametric network  $q_\theta$ , trained to approximate this posterior, produces  $K$  completions

$$\hat{F}_{\text{uno}}^{(k)} \sim q_\theta(I), \quad k = 1, \dots, K. \quad (1)$$

When the model is deterministic,  $q_\theta$  collapses to a point estimate ( $K=1$ ).

#### 3.2 Estimating the Observed Floormap from an Egocentric View

As shown in Fig. 1, the observed BEV floormap is produced from a single RGB image by two deterministic operators [12]. A preprocessing stage  $\Phi$  extracts an image-plane depth map  $D$  via DepthPro [17] and a floor segmentation  $S$  via SegFormer [153] (trained on ADE-20K [163]). A projection stage  $\Psi$  then back-projects these signals into the BEV grid using camera intrinsics  $\mathbf{K}$  (metric depth is used directly when available), yielding the observed floormap  $F_{\text{obs}}$  and the observation footprint mask  $O$ :

$$(D, S) := \Phi(I), \quad (F_{\text{obs}}, O) := \Psi(D, S; \mathbf{K}). \quad (2)$$

Here  $O$  and  $U$  are the binary masks indicating membership in  $R_O$  and  $R_U$ , respectively. At inference, neither the camera pose nor the complete map is

**Table 1: Source datasets aggregated into FlatLands.** Obs. (raw) are upstream counts before quality filtering; Obs. (filtered) retain only observations with conditional signal ratio  $r_{\text{cond}} \geq 0.10$ . ScanNet++ is OOD test-only. Details can be found in Sec. S2.

Dataset	Scenes	Obs. (raw)	Obs. (filtered)	Asset Used
ZInD [34]	7,026	168,624	133,096	Panorama (see Sec. S2.1)
ARKitScenes [7]	4,803	115,271	40,282	PLY mesh
Matterport3D [24]	2,101	50,424	38,004	PLY mesh
ScanNet [36]	1,508	36,192	24,763	PLY mesh
3RScan [147]	1,291	30,984	18,216	OBJ mesh
ScanNet++ [160]	927	22,248	16,214	PLY mesh (OOD-only)
<b>FlatLands(Ours)</b>	<b>17,656</b>	<b>423,743</b>	<b>270,575</b>	4× binary 2D maps

available; completion models operate solely on the abstract BEV conditioning pair  $(F_{\text{obs}}, U)$ .

### 3.3 Training Floormap Completion Models

Stochastic models draw  $K > 1$  samples to represent posterior uncertainty. Each sample  $\hat{F}_{\text{uno}}^{(k)}$  is assembled into a full completion by preserving observed evidence exactly:

$$F_{\text{comp}}^{(k)} = F_{\text{obs}} + U \odot \hat{F}_{\text{uno}}^{(k)}. \quad (3)$$

This evidence-clamping step enforces a posterior support constraint: returned completions agree with  $F_{\text{obs}}$  on all observed cells while remaining free to vary over  $U$ . Models are supervised against the ground-truth floormap  $F^*$ , derived from scene meshes provided by the source datasets. The dataset also provides a valid-workspace mask  $V$  that distinguishes in-bounds cells from out-of-bounds or undefined regions. All losses and metrics are computed only on the unobserved valid evaluation region  $R_{\text{eval}} = U \odot V$ , so scores reflect completion quality beyond the camera frustum.

The canonical camera convention and deployed RGB-to-floormaps front-end are specified in Sec. S1.

## 4 FlatLands Dataset

*Sources, scope, and canonical splits.* FlatLands combines six real indoor metric datasets: Matterport3D [24], ScanNet [36], ScanNet++ [160], ARKitScenes [7], 3RScan [147], and ZInD [34], covering 17,656 unique scene layouts. We synthesize egocentric observations by sampling floor-valid camera centers and 24 yaw headings per center, with visibility computed via field-of-view and ray-occlusion tests. From 423,743 synthesized observations, filtering yields a canonical set of 270,575 observations (215,342 train, 26,890 val, 28,343 test; Fig. 2a), with ScanNet++ held out *entirely* as test-only OOD data. All splits are scene-disjoint. Source aggregation is summarized in Tab. 1 with source-wise breakdown in Fig. 2a.

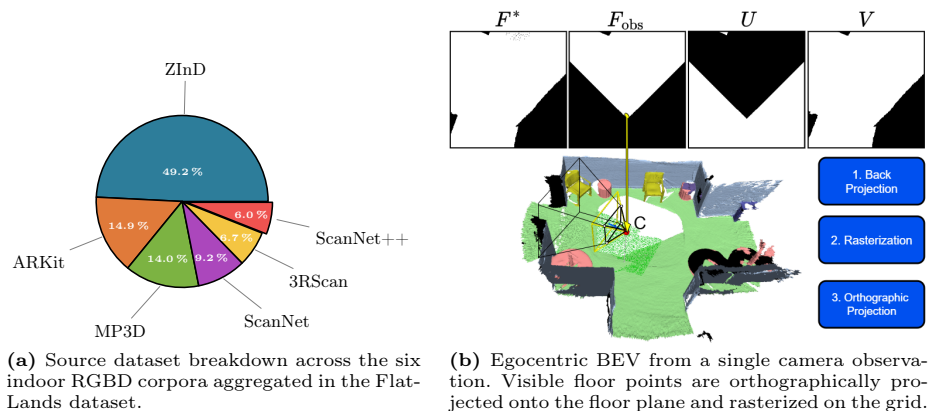


**Fig. 2:** FlatLands dataset statistics and construction.

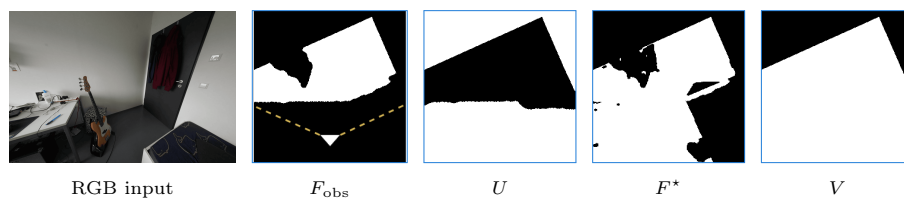


**Fig. 3:** Input egocentric RGB (left) and the four aligned  $256 \times 256$  binary maps per observation.  $F_{\text{obs}}$ : observed floor;  $U$ : valid unobserved;  $F^*$ : full floor ground truth;  $V$ : valid workspace. The white marker ( $\blacktriangledown$ ) denotes the fixed camera anchor in BEV.

*Data construction pipeline.* Each observation is generated offline by placing a virtual camera in the reconstructed 3D mesh at the sampled pose, back-projecting the rendered view, and orthogonally projecting the visible floor into a  $256 \times 256$  egocentric BEV grid as shown in Fig. 2b. The agent’s understanding of its pose in the world is not assumed at inference (egocentric). Full processing details, including observation synthesis and crop validation, are in Secs. S2, S2.2 and S2.4.

The pipeline outputs four aligned binary maps per observation (Fig. 3):  $F_{\text{obs}}$  (observed floor),  $U$  (valid but unobserved),  $F^*$  (full floor ground truth), and  $V$  (valid workspace). By construction,  $F_{\text{obs}} \cup U \subseteq V$ . Depth and mesh assets are used only offline: floor evidence comes from mesh plane-fitting for five datasets and from  $\text{DA}^2$  metric depth [70] for ZInD panoramas, calibrated via room-vertex annotations. Camera intrinsics, anchor convention, and grid resolution are fixed, enabling consistent difficulty interpretation across sources and ID/OOD subsets.

Source-specific processing, aggregation and filtering rules are in Secs. S2.1 and S2.4; split consistency and scene-level statistics are in Sec. S2.5. On  $R_{\text{eval}}$ , floor prevalence is moderately high (mean  $\approx 0.80$ ); its effect on metric ranking is analyzed in Sec. S2.4. Canonical tensors use a  $256 \times 256$  grid at 25.6 px/m, i.e.,  $\Delta \approx 0.039$  m per pixel; the cell-size rationale is explained in Secs. S2.3 and S2.4.

## 5 Experiments

We benchmark 11 methods spanning parameter-free approaches, deterministic completion, an epistemic ensemble, and stochastic posterior samplers. To isolate modeling effects, all learned methods share the same interface and evaluation protocol: inputs are  $(F_{\text{obs}}, U)$ ; losses and metrics are computed on the common supervision mask  $R_{\text{eval}}$ . A compact per-method summary is provided in Table 2.

### 5.1 Baselines

*Naive baselines.* Four parameter-free methods provide reference fill strategies for  $U$ , then are merged with observed evidence using the hard-clamp rule [86] (Eq. (3)). **All Obstacle** predicts obstacle (0) everywhere on  $U$ . **All Floor** predicts floor (1) everywhere on  $U$ . **NN Propagation** assigns an unobserved cell the label of the nearest observed one. **Uniform Random** samples i.i.d. Bernoulli(0.5) labels per cell.

*Deterministic models.* We evaluate **UNet** [117, 151], **PartialConv UNet** [79], and **LaMa** [31, 135]. All three keep their original backbones; we only adapt the input and output channels to binary BEV floor completion. UNet and PConv UNet are trained with masked BCE reconstruction losses on  $R_{\text{eval}}$ , while LaMa retains its reconstruction-plus-adversarial objective. At inference, continuous outputs are binarized via fixed thresholding [27] and then hard-clamped to preserve observed evidence [86].

*Stochastic models.* **LaMa Ensemble** trains four independent LaMa models with different random seeds [4, 51] and returns one output from each member ( $K=4$ ), providing seed-based diversity. Increasing the number of ensemble samples requires retraining a model on a different seed. We also evaluate three posterior conditional samplers: **Diffusion** [52, 127], **Flow Matching** [76, 77, 81], and **Flow Matching with Cross-Attention Conditioning (FM+XAttn)**. FM+XAttn keeps the baseline concatenated input and adds a condition encoder on  $[F_{\text{obs}}, U]$ , with cross-attention [146] injected only at coarse resolutions ( $64 \times 64$  and  $32 \times 32$ ), following modular conditioning ideas [102, 116, 162]. Operating cross-attention at coarse resolutions keeps parameter overhead modest while letting the generator attend to global layout cues from the conditioning pair; fine-grained spatial detail is resolved by the convolutional decoder. All three samplers share the same setup: masked BCE on  $R_{\text{eval}}$ , classifier-free guidance ( $s=2.0$ ) [37, 53], per-step evidence clamping [32, 115],  $K=4$  samples, and iterative sampling (50 DDIM steps for Diffusion, 50 Heun steps for Flow Matching, 25 Heun steps for FM+XAttn [50, 62, 127]).

*Implementation and reproducibility.* All models are trained in distributed full-precision mode on  $4 \times$  A100 40 GB GPUs under identical schedules; inference runs on consumer-grade hardware (Nvidia RTX 4090). Further architecture, training, and sampling details are reported in Secs. S5 and S8.2 and Tab. S12.

**Table 2: Baseline catalog.** Unless noted, learned methods share inputs ( $F_{\text{obs}}, U$ ), supervision mask  $R_{\text{eval}}$ , and hard evidence clamping before evaluation.

Method	Adaptations	Inference
<i>All naive baselines</i>	All-Obstacle (fill 0), All-Floor (fill 1), NN Propagation (nearest-observed copy), Uniform Random ( $p=0.5$ ). Parameter-free rules on $U$ ; merged with observed evidence via hard clamping (Eq. (3)).	Single pass
U-Net [117, 151]	Masked BCE on $R_{\text{eval}}$ . Backbone unchanged; binary BEV I/O only.	Thr. 0.5 + clamp
PConv-UNet [79]	Masked BCE on $R_{\text{eval}}$ . Partial-conv. mask propagation retained; adapted to binary BEV completion.	Thr. 0.5 + clamp
LaMa [31, 135]	Recon. + adversarial. Fourier-conv. generator retained; channels remapped for floor-occupancy completion.	Thr. 0.5 + clamp
LaMa Ens. [4, 51]	Same as LaMa (4 seeds). Epistemic variant from independent seed training; no architecture change.	$K=4$
Diffusion [52, 127]	Masked BCE on $R_{\text{eval}}$ . Posterior inpainting with per-step evidence clamping [32, 115].	DDIM, 50 st., CFG $s=2$
Flow Match. [76]	Masked BCE on $R_{\text{eval}}$ . Same conditioning/clamping as Diffusion; ODE transport parameterization.	Heun, 50 st., CFG $s=2$
FM+XAttn [76, 146]	Masked BCE on $R_{\text{eval}}$ . Adds condition encoder on $[F_{\text{obs}}, U]$ with cross-attn. ( $64 \times 64, 32 \times 32$ ); see [102, 116, 162].	Heun, 25 st., CFG $s=2$

The source code, pre-trained weights, and the full dataset reproduction pipeline will be publicly released.

## 5.2 Evaluation Protocol

We evaluate on the canonical test split ( $N=28,343$ ), partitioned into 12,129 in-distribution observations and 16,214 out-of-distribution observations. Quantitative results are computed on standardized BEV-conditioned inputs. Difficulty-tier and threshold analyses are in Sec. S2.5. All metrics are computed on the unobserved valid region  $R_{\text{eval}} = U \odot V$ . We additionally report the standard metrics IoU and F1 with traversable floor as the positive class (see Sec. S6). For this benchmark, we introduce two new metrics—UMR and MES—designed to calibrate fidelity and diversity under masked evaluation.

*Unobserved-region mismatch rate.* We define the unobserved-region mismatch rate (UMR; lower is better) as the fraction of misclassified cells on  $R_{\text{eval}}$ :

$$\text{UMR} = \frac{\text{FP} + \text{FN}}{|R_{\text{eval}}|} = 1 - \frac{\text{TP} + \text{TN}}{|R_{\text{eval}}|}. \quad (4)$$

Since floor prevalence on  $R_{\text{eval}}$  is high ( $\approx 0.80$ ; a natural bias in indoor spaces; see Sec. S2.4 for details), IoU and F1 primarily reflect floor-completion fidelity and can remain high even when wall boundaries are imperfect.

*Masked Energy Score.* For multi-sample methods, we introduce the Masked Energy Score (MES; lower is better) [46, 114]:

$$\text{MES} = \frac{1}{K} \sum_{k=1}^K d_{R_{\text{eval}}} \left( F_{\text{comp}}^{(k)}, F^* \right) - \frac{1}{2K(K-1)} \sum_{k \neq \ell} d_{R_{\text{eval}}} \left( F_{\text{comp}}^{(k)}, F_{\text{comp}}^{(\ell)} \right), \quad (5)$$

**Table 3:** Fidelity metrics (mean±std) on  $R_{\text{eval}}$  with oracle best-of- $K$  ( $K=4$ ) variant for stochastic methods (bottom four rows).

Method	ID			OOD		
	UMR↓	IoU↑	F1↑	UMR↓	IoU↑	F1↑
All-Obstacle	0.661 ± 0.229	0.000 ± 0.000	0.000 ± 0.000	0.854 ± 0.155	0.000 ± 0.000	0.000 ± 0.000
All-Floor	0.339 ± 0.229	0.661 ± 0.229	0.737 ± 0.210	0.146 ± 0.155	0.854 ± 0.155	0.912 ± 0.116
NN Prop.	0.243 ± 0.078	0.620 ± 0.219	0.708 ± 0.202	0.198 ± 0.156	0.779 ± 0.186	0.861 ± 0.143
Uniform Rand.	0.501 ± 0.002	0.367 ± 0.104	0.516 ± 0.128	0.502 ± 0.003	0.453 ± 0.057	0.621 ± 0.064
U-Net	0.122 ± 0.030	0.763 ± 0.132	0.843 ± 0.098	0.114 ± 0.111	0.870 ± 0.136	0.924 ± 0.094
PConv-UNet	0.126 ± 0.033	0.758 ± 0.132	0.838 ± 0.098	0.114 ± 0.113	0.870 ± 0.139	0.924 ± 0.097
LaMa	0.209 ± 0.059	0.623 ± 0.161	0.734 ± 0.131	0.283 ± 0.159	0.672 ± 0.190	0.787 ± 0.153
LaMa-Ens.	0.105 ± 0.099	0.817 ± 0.205	0.882 ± 0.154	0.107 ± 0.094	0.874 ± 0.126	0.927 ± 0.083
Diffusion	<b>0.099 ± 0.097</b>	<b>0.830 ± 0.196</b>	<b>0.892 ± 0.143</b>	<b>0.094 ± 0.092</b>	<b>0.890 ± 0.122</b>	<b>0.936 ± 0.082</b>
Flow Match.	0.100 ± 0.095	0.829 ± 0.192	<b>0.892 ± 0.139</b>	0.102 ± 0.099	0.880 ± 0.129	0.930 ± 0.088
FM+XAttn	0.100 ± 0.094	<b>0.830 ± 0.192</b>	<b>0.892 ± 0.139</b>	0.109 ± 0.092	0.873 ± 0.124	0.927 ± 0.084

**Table 4:** Stochastic evaluation (mean±std) on  $R_{\text{eval}}$  for  $K=4$ . MES: Masked Energy Score; IoU $_m$ : mean-of- $K$  IoU; Var: average per-pixel variance.

Method	ID			OOD		
	MES↓	IoU $_m$ ↑	Var↓	MES↓	IoU $_m$ ↑	Var↓
LaMa-Ens.	0.158 ± 0.139	0.713 ± 0.246	0.076 ± 0.062	0.149 ± 0.093	0.720 ± 0.155	0.084 ± 0.043
Diffusion	0.143 ± 0.152	0.763 ± 0.222	0.044 ± 0.029	0.097 ± 0.102	<b>0.832 ± 0.124</b>	0.048 ± 0.026
Flow Match.	0.143 ± 0.148	<b>0.766 ± 0.226</b>	<b>0.037 ± 0.029</b>	0.101 ± 0.103	<b>0.832 ± 0.135</b>	<b>0.043 ± 0.028</b>
FM+XAttn	<b>0.133 ± 0.138</b>	<b>0.766 ± 0.218</b>	0.044 ± 0.032	<b>0.095 ± 0.093</b>	0.813 ± 0.123	0.061 ± 0.028

with  $d_{R_{\text{eval}}}(A, B) = 1 - \text{IoU}_{R_{\text{eval}}}(A, B)$  (Jaccard distance [75]), which normalizes by the union and shares the same geometric semantics as the fidelity axis (see Sec. S6). The first term penalizes distance to the ground truth (fidelity); the second rewards pairwise spread among samples (diversity). We set  $K = 4$  (Sec. S7.2); sample-count sensitivity is analyzed in Sec. S7.2. Main tables report mean±std. We also report mean IoU, best-of- $K$  IoU, and per-pixel variance for the stochastic methods. For fairness, all methods use identical post-processing: fixed map thresholding [27], evidence hard clamping, and the common evaluation mask  $R_{\text{eval}}$ , preventing protocol differences from affecting model ranking. Downstream integration into closed-loop planners is an important direction but lies beyond the scope of this benchmark; we focus on fidelity and calibration of the completion stage itself.

## 6 Results and Discussion

Table 3 reports UMR, IoU, and F1 (mean±std) on  $R_{\text{eval}}$ . Among deterministic predictors on the ID split, UNet and PConv UNet lead, while LaMa trails—consistent with adversarial training trading distortion for perceptual realism [16]. The trivial All Floor baseline reaches IoU comparable to LaMa because high floor prevalence ( $\sim 0.80$ ; Sec. S2.4) inflates IoU for optimistic guesses (Sec. 5.2); NN Propagation ranks lower because nearest-neighbor copying replicates boundary pixels, lowering recall.

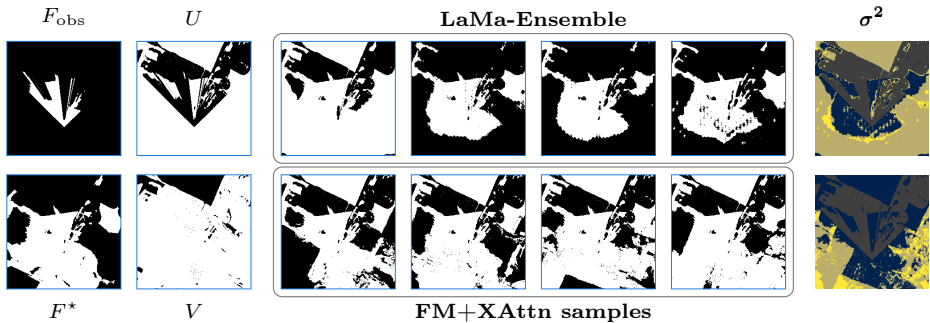


**Fig. 4:** LaMa-Ensemble vs. FM+XAttn on a multi-room ScanNet scene. **Row 1:** observed floor  $F_{\text{obs}}$  and unobserved mask  $U$  condition both models; the four LaMa-Ensemble samples (boxed) and their per-pixel variance  $\sigma^2$ . **Row 2:** ground-truth floor  $F^*$  and validity mask  $V$  used for evaluation; four FM+XAttn samples (boxed) and their  $\sigma^2$ . LaMa-Ensemble spreads variance uniformly; FM+XAttn concentrates it at layout boundaries.

With oracle best-of- $K$  selection ( $K=4$ ), all stochastic generators surpass every deterministic predictor, confirming that posterior sampling recovers higher-fidelity completions. Method ordering is stable despite per-scene variance, with stochastic best-of- $K$  reducing UMR furthest. Oracle selection is a standard diagnostic for posterior coverage [46, 66]; the oracle-free MES in Tab. 4 confirms the same ranking without privileged access to the ground truth. On the OOD split (ScanNet++), all methods improve in IoU and the ID ranking is preserved (Sec. S7), validating cross-source generalization. Since ScanNet++ contains room geometries and capture conditions unseen during training, the preserved ranking indicates that learned layout priors transfer across architectural styles rather than overfitting to source-specific artifacts. Additional quantitative analysis is reported in Sec. S4. Table 4 shows FM+XAttn achieves the best MES on both splits, with Flow Matching and Diffusion close behind and LaMa-Ensemble trailing. Mean-of- $K$  IoU is nearly identical across continuous generators, so differences lie in calibration rather than posterior mean accuracy; FM+XAttn trades slightly higher variance for improved calibration.

*Boundary variance.* Following Cheng *et al.* [29], we partition unobserved floor pixels into an interior set  $\Omega_{\text{int}}$  ( $\geq 7$  px from GT non-floor) and a boundary set  $\Omega_{\text{bnd}}$  (within 7 px of a floor–non-floor transition; justification in Sec. S3). A calibrated sampler should produce near-zero variance on  $\Omega_{\text{int}}$ ; boundary variance reflects genuine layout ambiguity. FM+XAttn attains  $\bar{\sigma}_{\text{int}}^2 = 6 \times 10^{-5}$ ,  $\bar{\sigma}_{\text{bnd}}^2 = 0.037$  (ratio  $\sim 600\times$ ), concentrating uncertainty at boundaries. LaMa-Ensemble yields  $\bar{\sigma}_{\text{int}}^2 = 0.052$  and  $\bar{\sigma}_{\text{bnd}}^2 = 0.125$  (ratio  $2.4\times$ ): its interior variance is  $\sim 880\times$  larger than that of FM+XAttn, indicating seed-level divergence rather than posterior ambiguity (see Fig. 4). FM+XAttn thus localizes uncertainty to genuinely ambiguous boundaries, whereas LaMa-Ensemble inflates variance in geometri-

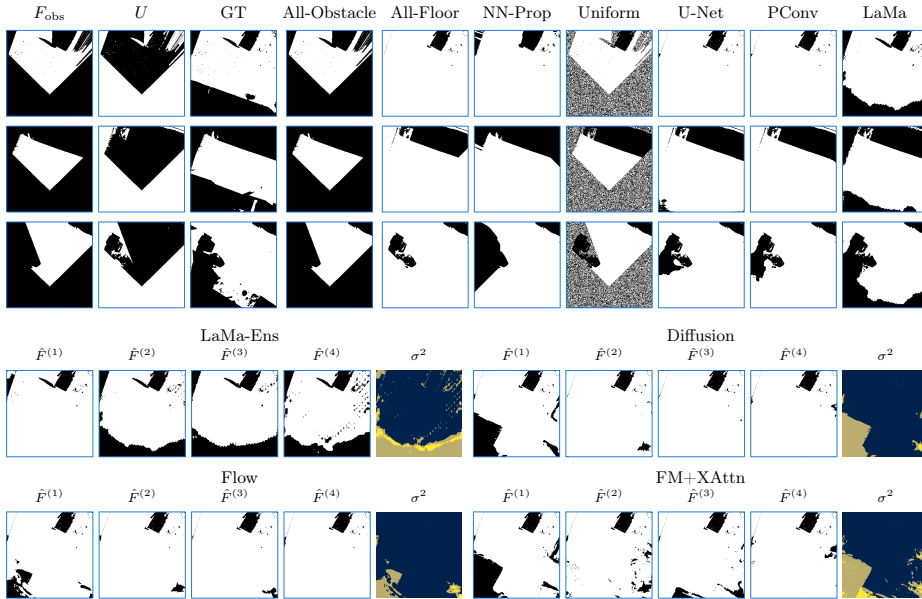


**Fig. 5: Qualitative results on the test split. Top:** deterministic single-output comparison across three scenes (in-distribution rows 1–2, out-of-distribution row 3). Columns show the observed floor  $F_{\text{obs}}$ , unobserved mask  $U$ , ground truth, and predictions from each baseline. These BEV observations are geometrically projected from the 3D mesh and do not involve any RGB input. **Bottom:** four independent samples, drawn from each stochastic generator for one in-distribution scene, alongside the per-pixel variance  $\sigma^2$  (brighter = higher disagreement).

cally determined interiors, raising MES. For a downstream planner, boundary-concentrated uncertainty is directly actionable: high-variance cells flag regions where collision risk is ambiguous and information-gathering actions would reduce planning uncertainty most.

*Qualitative observations.* Figure 5 shows representative test scenes: deterministic models are sharp in open regions but hallucinate non-floors at structural ambiguities, whereas stochastic generators spread mass across plausible layouts and highlight decision-relevant uncertainty (extended in Sec. S7).

Fig. 6 evaluates the monocular RGB→floormaps pipeline on held-out ScanNet++ images using Depth Pro [17] and SegFormer [153]. All learned models remain coherent under estimated BEV conditioning, confirming transfer from ground-truth inputs. The front-end projection introduces partial-depth artifacts and frustum-edge gaps, yet stochastic generators still produce plausible room extensions where deterministic methods truncate or fragment the floor. Comparing variance maps between Fig. 5 and Fig. 6, front-end noise slightly inflates interior variance but boundary-concentrated structure is preserved, indicating layout priors robust to moderate input corruption. Additional quantitative results, in-

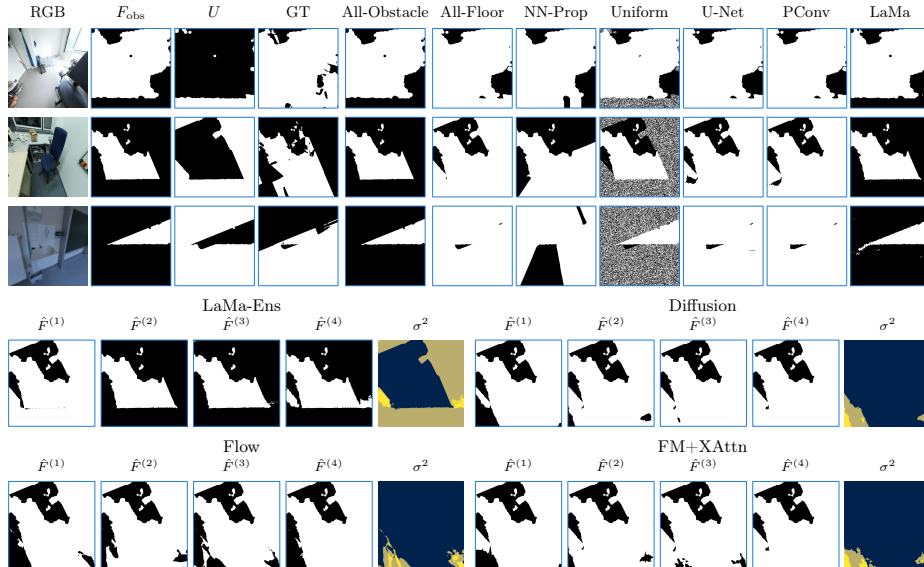


**Fig. 6: End-to-end inference pipeline results (RGB input).** **Top:** deterministic single-output comparison across three ScanNet++ scenes processed through the full monocular RGB→floormaps pipeline (Fig. 1). The RGB column shows the input egocentric image; the projected  $F_{\text{obs}}$  is noisier than the mesh-derived case (Fig. 5), increasing completion difficulty. **Bottom:** four independent posterior samples  $\hat{F}_{\text{uno}}^{(k)}$ ,  $k=1, \dots, 4$ , drawn from each stochastic generator for one scene, alongside the per-pixel variance  $\sigma^2$  (brighter = higher disagreement).

cluding end-to-end quantitative results, a synthetic ambiguity study when the true posterior under evaluation is fixed, and further qualitative examples are in Secs. S4 and S7. These observations hold under favorable conditioning; we next examine how all methods degrade when conditioning becomes scarce.

*Failure modes.* Fig. 7 isolates a hard case where a broad occlusion wedge leaves over half the GT floor outside the observation (red overlay:  $F^* \setminus F_{\text{obs}}$ ). Because no conditioning signal constrains this region, floor-boundary placement is geometrically under-determined, and most methods exhibit boundary leakage—over-extending floor into obstacle-heavy areas. In this specific case LaMa instead collapses (IoU = 0.003): with sparse conditioning, its adversarial objective becomes unstable—the discriminator trivially rejects large-region completions, causing the generator to mode-collapse to near-zero output [47]. Two additional failure patterns appear in the extended grid (Sec. S7.3): disconnected floor islands from sparse conditioning, and residual boundary artifacts in otherwise high-IoU scenes.

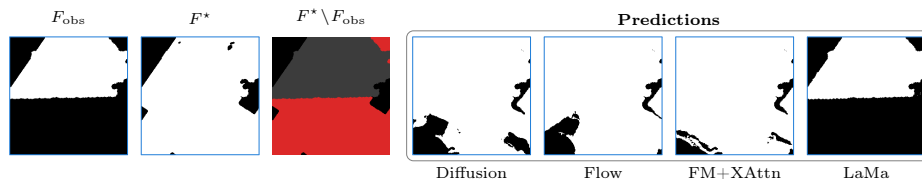


**Fig. 7: Failure case: boundary leakage under wide occlusion.** The red overlay ( $F^* \setminus F_{\text{obs}}$ ) highlights GT floor absent from the observation—over half the true floor here—leaving boundary placement geometrically under-determined. All generative methods over-extend floor into this ambiguous region; FM+XAttn is most conservative but residual leakage persists. LaMa collapses entirely (IoU = 0.003); one such other example of collapse is in Fig. 6 row 3. Extended grid in Sec. S7.3.

## 7 Conclusion: Limitations & Future Work

We presented a unified benchmark for single-view BEV floor completion with identical conditioning, masking, and scoring across deterministic, ensemble, and stochastic methods, with explicit ID and OOD splits. Three findings emerge: (1) stochastic generators with oracle selection surpass all deterministic predictors, confirming that posterior sampling recovers completions no single-pass estimator can match; (2) FM+XAttn concentrates variance at layout boundaries while ensemble seeds diverge globally—epistemic spread is a poor proxy for aleatoric layout ambiguity; (3) method ordering is preserved on the OOD split, indicating stable generalization.

This benchmark targets *binary* traversability only, without semantic cues [8, 129, 166], and assumes simplified pinhole intrinsics that do not capture the diversity of real robotic cameras. It also omits *graded* traversability (*e.g.* stairs, slopes, *etc.*), which would better reflect the feasible traversability constraints of heterogeneous embodied platforms like mobile, legged, or aerial robots. Failure analysis (Fig. 7; Sec. S7.3) indicates that when most ground-truth floor is unobserved, boundary placement becomes under-determined; consequently, all methods produce local defects poorly captured by IoU alone. Promising directions include expanding the source datasets to improve architectural diversity and building typologies; extending to multi-storey and multi-room settings; incorporating RGB and semantic cues for conditioning; adopting traversability definitions for different robotic systems; exploring modern backbones [28, 39, 101, 146, 154, 157]; and moving beyond single-view input to multi-view settings. Ethical considerations are discussed in Sec. S9.

Completed floorplans can serve as probabilistic spatial priors for belief-space planning [12, 35, 48, 68], active perception [45, 110], SLAM back-ends [19, 40, 89, 120], and generative motion planning [20, 85, 134, 137]. Because the representation is an abstract binary grid, the completion stage is sensor-agnostic. Closed-loop evaluation under map uncertainty [35, 104, 121] is a natural next step extending to planning and navigation [4, 14, 51].

## References

1. Austin, J., Johnson, D.D., Ho, J., Tarlow, D., van den Berg, R.: Structured Denoising Diffusion Models in Discrete State-Spaces. In: *Advances in Neural Information Processing Systems (NeurIPS)* (2021)
2. Axelrod, B., Kaelbling, L.P., Lozano-Pérez, T.: Provably Safe Robot Navigation with Obstacle Uncertainty. *The International Journal of Robotics Research* (2018)
3. Aydemir, A., Jensfelt, P., Folkesson, J.: What Can We Learn from 38,000 Rooms? Reasoning about Unexplored Space in Indoor Environments. In: *Proceedings of the IEEE/RSJ International Conference on Intelligent Robots and Systems (IROS)* (2012)
4. Baek, S., Moon, B., Kim, S., Cao, M., Ho, C., Scherer, S., Jeon, J.: PIPE Planner: Pathwise information gain with map predictions for indoor robot exploration. In: *Proceedings of the IEEE/RSJ International Conference on Intelligent Robots and Systems (IROS)* (2025)
5. Banfi, J., Woo, L., Campbell, M.: Is it Worth to Reason about Uncertainty in Occupancy Grid Maps during Path Planning? In: *Proceedings of the IEEE International Conference on Robotics and Automation (ICRA)* (2022)
6. Barrow, H.G., Tenenbaum, J.M., Bolles, R.C., Wolf, H.C.: Parametric Correspondence and Chamfer Matching: Two New Techniques for Image Matching. In: *International Joint Conference on Artificial Intelligence (IJCAI)* (1977)
7. Baruch, G., Chen, Z., Dehghan, A., Dimry, T., Feigin, Y., Fu, P., Gebauer, T., Kurz, D., Joffe, B., Schwartz, A., Shulman, E.: ARKitScenes: A diverse real-world dataset for 3D indoor scene understanding using mobile RGB-D data. In: *Advances in Neural Information Processing Systems (NeurIPS), Datasets and Benchmarks Track* (2021)
8. Behley, J., Garbade, M., Milioto, A., Quenzel, J., Behnke, S., Stachniss, C., Gall, J.: SemanticKITTI: A dataset for semantic scene understanding of LiDAR sequences. In: *Proceedings of the IEEE/CVF International Conference on Computer Vision (ICCV)* (2019)
9. Bengio, Y., Léonard, N., Courville, A.: Estimating or Propagating Gradients Through Stochastic Neurons for Conditional Computation. *arXiv preprint arXiv:1308.3432* (2013)
10. Bercher, P., Alford, R., Höller, D.: A Survey on Hierarchical Planning – One Abstract Idea, Many Concrete Realizations. In: *Proceedings of the International Joint Conference on Artificial Intelligence (IJCAI)* (2019)
11. Bertalmio, M., Sapiro, G., Caselles, V., Ballester, C.: Image Inpainting. In: *Proceedings of the 27th Annual Conference on Computer Graphics and Interactive Techniques (SIGGRAPH)* (2000)
12. Bhattacharjee, S.S., Lu, H., Campbell, D., Shome, R.: Into the Unknown: Towards using generative models for sampling priors of environment uncertainty for planning in configuration spaces. *arXiv preprint arXiv:2510.11014* (2025)
13. Bhattacharjee, S.S., Campbell, D., Shome, R.: Believing is Seeing: Unobserved Object Detection using Generative Models. In: *Proceedings of the IEEE/CVF Conference on Computer Vision and Pattern Recognition (CVPR)* (2025)
14. Bircher, A., Kamel, M., Alexis, K., Oleynikova, H., Siegwart, R.: Receding Horizon "Next-Best-View" Planner for 3D Exploration. In: *Proceedings of the IEEE International Conference on Robotics and Automation (ICRA)* (2016)
15. Black Forest Labs, Batifol, S., Blattmann, A., Boesel, F., Consul, S., Diagne, C., Dockhorn, T., English, J., English, Z., Esser, P., Kulal, S., Lacey, K., Levi, Y., Li,

- C., Lorenz, D., Müller, J., Podell, D., Rombach, R., Saini, H., Sauer, A., Smith, L.: FLUX.1 Kontext: Flow matching for in-context image generation and editing in latent space. arXiv preprint arXiv:2506.15742 (2025)
16. Blau, Y., Michaeli, T.: The Perception-Distortion Tradeoff. In: Proceedings of the IEEE/CVF Conference on Computer Vision and Pattern Recognition (CVPR) (2018)
  17. Bochkovskii, A., Delaunoy, A., Germain, H., Santos, M., Zhou, Y., Richter, S.R., Koltun, V.: Depth Pro: Sharp Monocular Metric Depth in Less Than a Second. In: International Conference on Learning Representations (ICLR) (2025)
  18. Bunse-Gerstner, A., Byers, R., Mehrmann, V., Nichols, N.K.: Numerical computation of an analytic singular value decomposition of a matrix valued function. *Numerische Mathematik* (1991)
  19. Cadena, C., Carlone, L., Carrillo, H., Latif, Y., Scaramuzza, D., Neira, J., Reid, I., Leonard, J.J.: Past, Present, and Future of Simultaneous Localization and Mapping: Toward the Robust-Perception Age. *IEEE Transactions on Robotics* (2016)
  20. Carvalho, J., Le, A.T., Baierl, M., Koert, D., Peters, J.: Motion Planning Diffusion: Learning and Planning of Robot Motions with Diffusion Models. In: Proceedings of the IEEE/RSJ International Conference on Intelligent Robots and Systems (IROS) (2023)
  21. Carvalho, J., Le, A.T., Kicki, P., Koert, D., Peters, J.: Motion Planning Diffusion: Learning and Adapting Robot Motion Planning with Diffusion Models. *IEEE Transactions on Robotics* (2025)
  22. Chan, E.R., Nagano, K., Chan, M.A., Bergman, A.W., Park, J.J., Levy, A., Aitala, M., Mello, S.D., Karras, T., Wetzstein, G.: Generative Novel View Synthesis with 3D-Aware Diffusion Models. In: Proceedings of the IEEE/CVF International Conference on Computer Vision (ICCV) (2023)
  23. Chan, T.F., Shen, J.: Nontexture Inpainting by Curvature-Driven Diffusions. *Journal of Visual Communication and Image Representation* (2001)
  24. Chang, A.X., Dai, A., Funkhouser, T., Halber, M., Niekner, M., Savva, M., Song, S., Zeng, A., Zhang, Y.: Matterport3D: Learning from RGB-D data in indoor environments. In: International Conference on 3D Vision (3DV) (2017)
  25. Chen, J., Liu, C., Wu, J., Furukawa, Y.: Floor-SP: Inverse CAD for Floorplans by Sequential Room-wise Shortest Path. In: Proceedings of the IEEE/CVF International Conference on Computer Vision (ICCV) (2019)
  26. Chen, T., Xu, B., Zhang, C., Guestrin, C.: Training Deep Nets with Sublinear Memory Cost. arXiv preprint arXiv:1604.06174 (2016)
  27. Chen, T., Zhang, R., Hinton, G.: Analog bits: Generating discrete data using diffusion models with self-conditioning. In: International Conference on Learning Representations (ICLR) (2023)
  28. Chen, X., Mishra, N., Rohaninejad, M., Abbeel, P.: PixelSNAIL: An improved autoregressive generative model. In: Proceedings of the International Conference on Machine Learning (ICML) (2018)
  29. Cheng, B., Girshick, R., Dollár, P., Berg, A.C., Kirillov, A.: Boundary IoU: Improving object-centric image segmentation evaluation. In: Proceedings of the IEEE/CVF Conference on Computer Vision and Pattern Recognition (CVPR) (2021)
  30. Cheng, Y.C., Lin, C.H., Lee, H.Y., Ren, J., Tulyakov, S., Yang, M.H.: In&out: Diverse image outpainting via GAN inversion. In: Proceedings of the IEEE/CVF Conference on Computer Vision and Pattern Recognition (CVPR) (2022)

31. Chi, L., Jiang, B., Mu, Y.: Fast Fourier Convolution. In: Advances in Neural Information Processing Systems (NeurIPS) (2020)
32. Christopher, J.K., Baek, S., Fioretto, F.: Constrained Synthesis with Projected Diffusion Models. In: Advances in Neural Information Processing Systems (NeurIPS) (2024)
33. Chung, H., Kim, J., McCann, M.T., Klasky, M.L., Ye, J.C.: Diffusion Posterior Sampling for General Noisy Inverse Problems. In: International Conference on Learning Representations (ICLR) (2023)
34. Cruz, S., Hutchcroft, W., Li, Y., Khosravan, N., Boyadzhiev, I., Kang, S.B.: Zillow Indoor Dataset: Annotated floor plans with 360° panoramas and 3D room layouts. In: Proceedings of the IEEE/CVF Conference on Computer Vision and Pattern Recognition (CVPR) (2021)
35. Curtis, A., Matheos, G., Gothoskar, N., Mansinghka, V., Tenenbaum, J.B., Lozano-Pérez, T., Kaelbling, L.P.: Partially Observable Task and Motion Planning with Uncertainty and Risk Awareness. In: Robotics: Science and Systems (RSS) (2024)
36. Dai, A., Chang, A.X., Savva, M., Halber, M., Funkhouser, T., Nießner, M.: ScanNet: Richly-annotated 3D reconstructions of indoor scenes. In: Proceedings of the IEEE Conference on Computer Vision and Pattern Recognition (CVPR) (2017)
37. Dhariwal, P., Nichol, A.: Diffusion Models Beat GANs on Image Synthesis. In: Advances in Neural Information Processing Systems (NeurIPS) (2021)
38. Dice, L.R.: Measures of the amount of ecologic association between species. *Ecology* (1945)
39. Dosovitskiy, A., Beyer, L., Kolesnikov, A., Weissenborn, D., Zhai, X., Unterthiner, T., Dehghani, M., Minderer, M., Heigold, G., Gelly, S., Uszkoreit, J., Houlsby, N.: An Image is Worth 16x16 Words: Transformers for Image Recognition at Scale. In: International Conference on Learning Representations (ICLR) (2021)
40. Durrant-Whyte, H., Bailey, T.: Simultaneous Localization and Mapping: Part I. *IEEE Robotics & Automation Magazine* (2006)
41. Elfes, A.: Using Occupancy Grids for Mobile Robot Perception and Navigation. *Computer* (1989)
42. Fang, X., Garrett, C.R., Eppner, C., Lozano-Pérez, T., Kaelbling, L.P., Fox, D.: DiMSam: Diffusion Models as Samplers for Task and Motion Planning under Partial Observability. In: Proceedings of the IEEE/RSJ International Conference on Intelligent Robots and Systems (IROS) (2024)
43. Fischler, M.A., Bolles, R.C.: Random Sample Consensus: A Paradigm for Model Fitting with Applications to Image Analysis and Automated Cartography. *Communications of the ACM* (1981)
44. Gal, Y., Ghahramani, Z.: Dropout as a Bayesian Approximation: Representing Model Uncertainty in Deep Learning. In: Proceedings of the International Conference on Machine Learning (ICML) (2016)
45. Garg, S., Sünderhauf, N., Dayoub, F., Morrison, D., Cosgun, A., Carneiro, G., Wu, Q., Chin, T.J., Reid, I., Gould, S., Corke, P., Milford, M.: Semantics for Robotic Mapping, Perception and Interaction: A Survey. *Foundations and Trends® in Robotics* (2020)
46. Gneiting, T., Raftery, A.E.: Strictly Proper Scoring Rules, Prediction, and Estimation. *Journal of the American Statistical Association* (2007)
47. Goodfellow, I.J., Pouget-Abadie, J., Mirza, M., Xu, B., Warde-Farley, D., Ozair, S., Courville, A., Bengio, Y.: Generative Adversarial Nets. In: Advances in Neural Information Processing Systems (NeurIPS) (2014)

48. Han, Y., Banfi, J., Campbell, M.: Planning Paths Through Unknown Space by Imagining What Lies Therein. In: Conference on Robot Learning (CoRL) (2020)
49. Hartley, R., Zisserman, A.: Multiple View Geometry in Computer Vision. Cambridge University Press (2004)
50. Heun, K.: Neue methode zur approximativen lösung der differentialgleichungen einer unabhängigen veränderlichen. Zeitschrift für Mathematik und Physik (1900)
51. Ho, C., Kim, S., Moon, B., Parandekar, A., Harutyunyan, N., Wang, C., Sycara, K., Best, G., Scherer, S.: MapEx: Indoor structure exploration with probabilistic information gain from global map predictions. In: Proceedings of the IEEE International Conference on Robotics and Automation (ICRA) (2025)
52. Ho, J., Jain, A., Abbeel, P.: Denoising Diffusion Probabilistic Models. In: Advances in Neural Information Processing Systems (NeurIPS) (2020)
53. Ho, J., Salimans, T.: Classifier-Free Diffusion Guidance. In: NeurIPS Workshop on Diffusion Models (2022)
54. Hollein, L., Cao, A., Owens, A., Johnson, J., Niessner, M.: Text2Room: Extracting Textured 3D Meshes from 2D Text-to-Image Models. In: Proceedings of the IEEE/CVF International Conference on Computer Vision (ICCV) (2023)
55. Hoogeboom, E., Heek, J., Salimans, T.: Simple Diffusion: End-to-End Diffusion for High Resolution Images. In: Proceedings of the International Conference on Machine Learning (ICML) (2023)
56. Hoogeboom, E., Nielsen, D., Jaini, P., Forré, P., Welling, M.: Argmax Flows and Multinomial Diffusion: Learning Categorical Distributions. In: Advances in Neural Information Processing Systems (NeurIPS) (2021)
57. Hornung, A., Wurm, K.M., Bennewitz, M., Stachniss, C., Burgard, W.: OctoMap: An efficient probabilistic 3D mapping framework based on octrees. Autonomous Robots (2013)
58. Hua, B.S., Pham, Q.H., Nguyen, D.T., Tran, M.K., Yu, L.F., Yeung, S.K.: SceneNN: A scene meshes dataset with annotations. In: International Conference on 3D Vision (3DV) (2016)
59. Jaccard, P.: Étude comparative de la distribution florale dans une portion des Alpes et des Jura. Bulletin de la Société Vaudoise des Sciences Naturelles (1901)
60. Johnson, J., Alahi, A., Fei-Fei, L.: Perceptual Losses for Real-Time Style Transfer and Super-Resolution. In: Proceedings of the European Conference on Computer Vision (ECCV) (2016)
61. Kaelbling, L.P., Littman, M.L., Cassandra, A.R.: Planning and Acting in Partially Observable Stochastic Domains. Artificial Intelligence (1998)
62. Karras, T., Aittala, M., Aila, T., Laine, S.: Elucidating the Design Space of Diffusion-Based Generative Models. In: Advances in Neural Information Processing Systems (NeurIPS) (2022)
63. Katsumata, Y., Kanechika, A., Taniguchi, A., Hafi, L.E., Hagiwara, Y., Taniguchi, T.: Map Completion from Partial Observation using the Global Structure of Multiple Environmental Maps. Advanced Robotics (2022)
64. Katyal, K., Popek, K., Paxton, C., Burlina, P., Hager, G.D.: Uncertainty-Aware Occupancy Map Prediction Using Generative Networks for Robot Navigation. In: Proceedings of the IEEE International Conference on Robotics and Automation (ICRA) (2019)
65. Kerbl, B., Kopanas, G., Leimkühler, T., Drettakis, G.: 3D Gaussian Splatting for Real-Time Radiance Field Rendering. ACM Transactions on Graphics (2023)
66. Kohl, S.A.A., Romera-Paredes, B., Meyer, C., Fauw, J.D., Ledsam, J.R., Maier-Hein, K.H., Eslami, S.M.A., Rezende, D.J., Ronneberger, O.: A Probabilistic U-

- Net for Segmentation of Ambiguous Images. In: *Advances in Neural Information Processing Systems (NeurIPS)* (2018)
67. Kuipers, B.: *The Spatial Semantic Hierarchy*. *Artificial Intelligence* (2000)
  68. Kurniawati, H.: *Partially Observable Markov Decision Processes and Robotics*. *Annual Review of Control, Robotics, and Autonomous Systems* (2022)
  69. LaValle, S.M.: *Planning Algorithms*. Cambridge University Press (2006)
  70. Li, H., Zheng, W., He, J., Liu, Y., Lin, X., Yang, X., Chen, Y.C., Guo, C.: DA<sup>2</sup>: Depth anything in any direction. In: *International Conference on Learning Representations (ICLR)* (2026)
  71. Li, J., Chen, C., Xiong, Z.: Contextual outpainting with object-level contrastive learning. In: *Proceedings of the IEEE/CVF Conference on Computer Vision and Pattern Recognition (CVPR)* (2022)
  72. Li, X., Qiu, H., Wang, L., Zhang, H., Qi, C., Han, L., Xiong, H., Li, H.: *Challenges and Trends in Egocentric Vision: A Survey*. *Machine Intelligence Research* (2026)
  73. Li, Z., Wang, W., Li, H., Xie, E., Sima, C., Lu, T., Qiao, Y., Dai, J.: BEVFormer: Learning Bird’s-Eye-View representation from multi-camera images via spatiotemporal transformers. In: *Proceedings of the European Conference on Computer Vision (ECCV)* (2022)
  74. Ling, L., Sheng, Y., Tu, Z., Zhao, W., Xin, C., Wan, K., Yu, L., Guo, Q., Yu, Z., Lu, Y., Li, X., Sun, X., Ashok, R., Mukherjee, A., Kang, H., Kong, X., Hua, G., Zhang, T., Benes, B., Bera, A.: DL3DV-10K: A large-scale scene dataset for deep learning-based 3D vision. In: *Proceedings of the IEEE/CVF Conference on Computer Vision and Pattern Recognition (CVPR)* (2024)
  75. Lipkus, A.H.: A proof of the triangle inequality for the Tanimoto distance. *Journal of Mathematical Chemistry* (1999)
  76. Lipman, Y., Chen, R.T.Q., Ben-Hamu, H., Nickel, M., Le, M.: Flow Matching for Generative Modeling. In: *International Conference on Learning Representations (ICLR)* (2023)
  77. Lipman, Y., Havasi, M., Holderrieth, P., Shaul, N., Le, M., Karrer, B., Chen, R.T.Q., Lopez-Paz, D., Ben-Hamu, H., Gat, I.: Flow Matching Guide and Code. *arXiv preprint arXiv:2412.06264* (2024)
  78. Liu, C., Wu, J., Furukawa, Y.: FloorNet: A unified framework for floorplan reconstruction from 3D scans. In: *Proceedings of the European Conference on Computer Vision (ECCV)* (2018)
  79. Liu, G., Reda, F.A., Shih, K.J., Wang, T.C., Tao, A., Catanzaro, B.: Image Inpainting for Irregular Holes Using Partial Convolutions. In: *Proceedings of the European Conference on Computer Vision (ECCV)* (2018)
  80. Liu, M., Xu, C., Jin, H., Gao, L., Tao, X., Li, Y.: One-2-3-45++: Fast Single Image to 3D Objects with Consistent Multi-View Generation and 3D Diffusion. In: *Proceedings of the IEEE/CVF Conference on Computer Vision and Pattern Recognition (CVPR)* (2024)
  81. Liu, X., Gong, C., Liu, Q.: Flow Straight and Fast: Learning to Generate and Transfer Data with Rectified Flow. In: *International Conference on Learning Representations (ICLR)* (2023)
  82. Liu, Y., Xu, K., Liu, Y., Liu, Y., He, J., Tong, R.: Acc3D: Accelerating Single Image to 3D Diffusion Models via Edge Consistency Guided Score Distillation. In: *Proceedings of the IEEE/CVF Conference on Computer Vision and Pattern Recognition (CVPR)* (2025)
  83. Loshchilov, I., Hutter, F.: SGDR: Stochastic gradient descent with warm restarts. In: *International Conference on Learning Representations (ICLR)* (2017)

84. Loshchilov, I., Hutter, F.: Decoupled Weight Decay Regularization. In: International Conference on Learning Representations (ICLR) (2019)
85. Lu, H., Kurniawati, H., Shome, R.: Sampling-Based Motion Planning for Optimal Probability of Collision under Environment Uncertainty. In: Proceedings of the IEEE/RSJ International Conference on Intelligent Robots and Systems (IROS) (2024)
86. Lugmayr, A., Danelljan, M., Romero, A., Yu, F., Timofte, R., Gool, L.V.: RePaint: Inpainting using denoising diffusion probabilistic models. In: Proceedings of the IEEE/CVF Conference on Computer Vision and Pattern Recognition (CVPR) (2022)
87. Luo, Z., Huang, W.: FloorPlanGAN: Vector residential floorplan adversarial generation. *Automation in Construction* (2022)
88. Maciejewski, A.A., Fox, J.J.: Path planning and the topology of configuration space. *IEEE Transactions on Robotics and Automation* (1993)
89. Maggio, D., Lim, H., Carlone, L.: VGGT-SLAM: Dense RGB SLAM optimized on the  $SL(4)$  manifold. In: Advances in Neural Information Processing Systems (NeurIPS) (2025)
90. Mildenhall, B., Srinivasan, P.P., Tancik, M., Barron, J.T., Ramamoorthi, R., Ng, R.: NeRF: Representing scenes as neural radiance fields for view synthesis. In: European Conference on Computer Vision (ECCV) (2020)
91. Miyato, T., Jaeger, B., Welling, M., Geiger, A.: GTA: A geometry-aware attention mechanism for multi-view transformers. In: International Conference on Learning Representations (ICLR) (2024)
92. Müller, M., Casser, V., Lahoud, J., Smith, N., Ghanem, B.: Learning to Find Good Correspondences for Image-Based Room Layout Estimation. In: Proceedings of the IEEE/CVF Conference on Computer Vision and Pattern Recognition (CVPR) (2018)
93. Müller, N., Schwarz, K., Rössl, B., Porzi, L., Bulò, S.R., Nießner, M., Kotschieder, P.: MultiDiff: Consistent novel view synthesis from a single image. In: Proceedings of the IEEE/CVF Conference on Computer Vision and Pattern Recognition (CVPR) (2024)
94. Mumford, D.: Pattern Theory: A Unifying Perspective. In: First European Congress of Mathematics, Paris, July 6–10, 1992, Vol. II. Birkhäuser Basel (1994)
95. Nichol, A.Q., Dhariwal, P.: Improved Denoising Diffusion Probabilistic Models. In: Proceedings of the International Conference on Machine Learning (ICML) (2021)
96. Oleynikova, H., Taylor, Z., Fehr, M., Siegwart, R., Nieto, J.: Voxblox: Incremental 3D euclidean signed distance fields for on-board MAV planning. In: Proceedings of the IEEE/RSJ International Conference on Intelligent Robots and Systems (IROS) (2017)
97. O’Meadhra, C., Tabib, W., Michael, N.: Variable Resolution Occupancy Mapping Using Gaussian Mixture Models. *IEEE Robotics and Automation Letters* (2019)
98. Papadakis, P.: Terrain Traversability Analysis Methods for Unmanned Ground Vehicles: A Survey. *Engineering Applications of Artificial Intelligence* (2013)
99. Pathak, D., Krähenbühl, P., Donahue, J., Darrell, T., Efros, A.A.: Context Encoders: Feature Learning by Inpainting. In: Proceedings of the IEEE Conference on Computer Vision and Pattern Recognition (CVPR) (2016)
100. Paulius, D., Sun, Y.: A Survey of Knowledge Representation in Service Robotics. *Robotics and Autonomous Systems* (2019)
101. Peebles, W., Xie, S.: Scalable Diffusion Models with Transformers. In: Proceedings of the IEEE/CVF International Conference on Computer Vision (ICCV) (2023)

102. Perez, E., Strub, F., de Vries, H., Dumoulin, V., Courville, A.: FiLM: Visual reasoning with a general conditioning layer. In: Proceedings of the AAAI Conference on Artificial Intelligence (AAAI) (2018)
103. Pillion, J., Fidler, S.: Lift, Splat, Shoot: Encoding Images from Arbitrary Camera Rigs by Implicitly Unprojecting to 3D. In: Proceedings of the European Conference on Computer Vision (ECCV) (2020)
104. Platt, R., Tedrake, R., Kaelbling, L.P., Lozano-Pérez, T.: Belief Space Planning Assuming Maximum Likelihood Observations. In: Robotics: Science and Systems (RSS) (2010)
105. Plizzari, C., Goletto, G., Furnari, A., Bansal, S., Ragusa, F., Farinella, G.M., Damen, D., Tommasi, T.: An Outlook into the Future of Egocentric Vision. *International Journal of Computer Vision (IJCV)* (2024)
106. Podell, D., English, Z., Lacey, K., Blattmann, A., Dockhorn, T., Müller, J., Penna, J., Rombach, R.: SDXL: Improving latent diffusion models for high-resolution image synthesis. In: International Conference on Learning Representations (ICLR) (2024)
107. Pronobis, A., Sjöö, K., Aydemir, A., Bishop, A.N., Jensfelt, P.: A Framework for Robust Cognitive Spatial Mapping. In: Proceedings of the International Conference on Advanced Robotics (ICAR) (2009)
108. Qi, S., Zhu, Y., Huang, S., Jiang, C., Zhu, S.C.: Human-centric Indoor Scene Synthesis Using Stochastic Grammar. In: Proceedings of the IEEE/CVF Conference on Computer Vision and Pattern Recognition (CVPR) (2018)
109. Rahman, M., Carneiro, G.: Hierarchical Probabilistic Ultrasound Image Inpainting via Variational Inference. In: Proceedings of the IEEE/CVF Conference on Computer Vision and Pattern Recognition (CVPR) (2023)
110. Ramakrishnan, S.K., Al-Halah, Z., Grauman, K.: Occupancy Anticipation for Efficient Exploration and Navigation. In: Proceedings of the European Conference on Computer Vision (ECCV) (2020)
111. Ramakrishnan, S.K., Gokaslan, A., Wijmans, E., Maksymets, O., Clegg, A., Turner, J., Undersander, E., Galuba, W., Westbury, A., Chang, A.X., Savva, M., Zhao, Y., Batra, D.: Habitat-Matterport 3D Dataset (HM3D): 1000 Large-Scale 3D Environments for Embodied AI. In: Advances in Neural Information Processing Systems (NeurIPS), Datasets and Benchmarks Track (2021)
112. Ramesh, A., Dhariwal, P., Nichol, A., Chu, C., Chen, M.: Hierarchical Text-Conditional Image Generation with CLIP Latents. arXiv preprint arXiv:2204.06125 (2022)
113. Reed, A., Crowe, B., Albin, D., Achey, L., Hayes, B., Heckman, C.: SceneSense: Diffusion models for 3D occupancy synthesis from partial observation. In: Proceedings of the IEEE/RSJ International Conference on Intelligent Robots and Systems (IROS) (2024)
114. Rizzo, M.L., Székely, G.J.: Energy Distance. *Wiley Interdisciplinary Reviews: Computational Statistics* (2016)
115. Rochman-Sharabi, O., Louppe, G.: Predict-Project-Renoise: Sampling Diffusion Models under Hard Constraints. arXiv preprint arXiv:2601.21033 (2026)
116. Rombach, R., Blattmann, A., Lorenz, D., Esser, P., Ommer, B.: High-Resolution Image Synthesis with Latent Diffusion Models. In: Proceedings of the IEEE/CVF Conference on Computer Vision and Pattern Recognition (CVPR) (2022)
117. Ronneberger, O., Fischer, P., Brox, T.: U-Net: Convolutional networks for biomedical image segmentation. In: Medical Image Computing and Computer-Assisted Intervention (MICCAI) (2015)

118. Rottmann, A., Mozos, Ó.M., Stachniss, C., Burgard, W.: Semantic Place Classification of Indoor Environments with Mobile Robots Using Boosting. In: Proceedings of the AAAI Conference on Artificial Intelligence (AAAI) (2005)
119. Sargent, K., Li, Z., Shah, T., Herrmann, C., Yu, H.X., Zhang, Y., Chan, E.R., Lagun, D., Fei-Fei, L., Sun, D., Wu, J.: ZeroNVS: Zero-shot 360-degree view synthesis from a single image. In: Proceedings of the IEEE/CVF Conference on Computer Vision and Pattern Recognition (CVPR) (2024)
120. Sarlin, P.E., DeTone, D., Malisiewicz, T., Rabinovich, A.: OrienterNet: Visual localization in 2D public maps with neural matching. In: Proceedings of the IEEE/CVF Conference on Computer Vision and Pattern Recognition (CVPR) (2023)
121. Savva, M., Kadian, A., Maksymets, O., Zhao, Y., Wijmans, E., Jain, B., Straub, J., Liu, J., Koltun, V., Malik, J., Parikh, D., Batra, D.: Habitat: A platform for embodied AI research. In: Proceedings of the IEEE/CVF International Conference on Computer Vision (ICCV) (2019)
122. Schmid, L., Cheema, M.N., Reijgwart, V., Siegwart, R., Tombari, F., Cadena, C.: SC-Explorer: Incremental 3D scene completion for safe and efficient exploration mapping and planning. arXiv preprint arXiv:2208.08307 (2022)
123. Schönberger, J.L., Frahm, J.M.: Structure-from-Motion Revisited. In: Proceedings of the IEEE Conference on Computer Vision and Pattern Recognition (CVPR) (2016)
124. Serifi, A., Grandia, R., Knoop, E., Gross, M., Bächer, M.: Robot Motion Diffusion Model: Motion Generation for Robotic Characters. In: SIGGRAPH Asia 2024 Conference Papers (SA '24) (2024)
125. Shabani, M.A., Hosseini, S., Furukawa, Y.: HouseDiffusion: Vector floorplan generation via a diffusion model with discrete and continuous denoising. In: Proceedings of the IEEE/CVF Conference on Computer Vision and Pattern Recognition (CVPR) (2023)
126. Silberman, N., Hoiem, D., Kohli, P., Fergus, R.: Indoor Segmentation and Support Inference from RGB-D Images. In: Proceedings of the European Conference on Computer Vision (ECCV) (2012)
127. Song, J., Meng, C., Ermon, S.: Denoising Diffusion Implicit Models. In: International Conference on Learning Representations (ICLR) (2021)
128. Song, S., Lichtenberg, S.P., Xiao, J.: SUN RGB-D: A RGB-D scene understanding benchmark suite. In: Proceedings of the IEEE Conference on Computer Vision and Pattern Recognition (CVPR) (2015)
129. Song, S., Yu, F., Zeng, A., Chang, A.X., Savva, M., Funkhouser, T.: Semantic Scene Completion from a Single Depth Image. In: Proceedings of the IEEE/CVF Conference on Computer Vision and Pattern Recognition (CVPR) (2017)
130. Song, Y., Shen, L., Xing, L., Ermon, S.: Solving Inverse Problems in Medical Imaging with Score-Based Generative Models. In: International Conference on Learning Representations (ICLR) (2022)
131. Song, Y., Sohl-Dickstein, J., Kingma, D.P., Kumar, A., Ermon, S., Poole, B.: Score-Based Generative Modeling through Stochastic Differential Equations. In: International Conference on Learning Representations (ICLR) (2021)
132. Souza, A., Gonçalves, L.M.G.: Occupancy-elevation grid: an alternative approach for robotic mapping and navigation. *Robotica* (2016)
133. Stuart, A.M.: Inverse Problems: A Bayesian Perspective. *Acta Numerica* (2010)
134. Su, C., Fu, Y., Hu, Z., Yang, J., Hanji, P., Wang, S., Zhao, X., Öztireli, C., Zhong, F.: CHORD: Generation of collision-free, house-scale, and organized digital twins

- for 3D indoor scenes with controllable floor plans and optimal layouts. arXiv preprint arXiv:2503.11958 (2025)
135. Suvorov, R., Logacheva, E., Mashikhin, A., Remizova, A., Ashukha, A., Silvestrov, A., Kong, N., Goka, H., Park, K., Lempitsky, V.: Resolution-Robust Large Mask Inpainting with Fourier Convolutions. In: Proceedings of the IEEE/CVF Winter Conference on Applications of Computer Vision (WACV) (2022)
  136. Székely, G.J., Rizzo, M.L.: Energy Statistics: A Class of Statistics Based on Distances. *Journal of Statistical Planning and Inference* (2013)
  137. Tang, J., Nie, Y., Markhasin, L., Dai, A., Thies, J., Nießner, M.: DiffuScene: Denoising diffusion models for generative indoor scene synthesis. In: Proceedings of the IEEE/CVF Conference on Computer Vision and Pattern Recognition (CVPR) (2024)
  138. Tarantola, A.: *Inverse Problem Theory and Methods for Model Parameter Estimation*. Society for Industrial and Applied Mathematics (2005)
  139. Telea, A.: An Image Inpainting Technique Based on the Fast Marching Method. *Journal of Graphics Tools* (2004)
  140. Tewari, A., Yin, T., Cazenavette, G., Rezhikov, S., Tenenbaum, J.B., Durand, F., Freeman, W.T., Sitzmann, V.: Diffusion with Forward Models: Solving Stochastic Inverse Problems Without Direct Supervision. In: *Advances in Neural Information Processing Systems (NeurIPS)* (2023)
  141. Thrun, S.: *Learning Metric-Topological Maps for Indoor Mobile Robot Navigation*. *Artificial Intelligence* (1998)
  142. Thrun, S.: *Robotic mapping: a survey*, p. 1–35. Morgan Kaufmann Publishers Inc., San Francisco, CA, USA (2003)
  143. Thrun, S., Bücken, A.: Integrating Grid-Based and Topological Maps for Mobile Robot Navigation. In: *Proceedings of the Thirteenth National Conference on Artificial Intelligence (AAAI-96)* (1996)
  144. Thrun, S., Burgard, W., Fox, D.: *Probabilistic Robotics*. MIT Press (2005)
  145. Tong, A., Fatras, K., Malkin, N., Huguet, G., Zhang, Y., Rector-Brooks, J., Wolf, G., Bengio, Y.: Improving and generalizing flow-based generative models with minibatch optimal transport. *Transactions on Machine Learning Research (TMLR)* (2024)
  146. Vaswani, A., Shazeer, N., Parmar, N., Uszkoreit, J., Jones, L., Gomez, A.N., Kaiser, L., Polosukhin, I.: Attention Is All You Need. In: *Advances in Neural Information Processing Systems (NeurIPS)* (2017)
  147. Wald, J., Avetisyan, A., Navab, N., Tombari, F., Nießner, M.: RIO: 3D object instance re-localization in changing indoor environments. In: *Proceedings of the IEEE/CVF International Conference on Computer Vision (ICCV)* (2019)
  148. Wang, J., Chen, M., Karaev, N., Vedaldi, A., Ruppel, C., Novotny, D.: VGGT: Visual geometry grounded transformer. In: *Proceedings of the IEEE/CVF Conference on Computer Vision and Pattern Recognition (CVPR)* (2025)
  149. Wang, Y., Tao, X., Shen, X., Jia, J.: Wide-Context Semantic Image Extrapolation. In: *Proceedings of the IEEE/CVF Conference on Computer Vision and Pattern Recognition (CVPR)* (2019)
  150. Wei, M., Lee, D., Isler, V., Lee, D.: Occupancy Map Inpainting for Online Robot Navigation. In: *Proceedings of the IEEE International Conference on Robotics and Automation (ICRA)* (2021)
  151. Wu, Y., He, K.: Group Normalization. In: *Proceedings of the European Conference on Computer Vision (ECCV)* (2018)

152. Xia, F., Zamir, A.R., He, Z.Y., Sax, A., Malik, J., Savarese, S.: Gibson Env: Real-world perception for embodied agents. In: Proceedings of the IEEE Conference on Computer Vision and Pattern Recognition (CVPR) (2018)
153. Xie, E., Wang, W., Yu, Z., Anandkumar, A., Alvarez, J.M., Luo, P.: SegFormer: Simple and efficient design for semantic segmentation with transformers. In: Advances in Neural Information Processing Systems (NeurIPS) (2021)
154. Xie, Z., Wei, Y., Cao, H., Zhao, C., Deng, C., Li, J., Dai, D., Gao, H., Chang, J., Yu, K., Zhao, L., Zhou, S., Xu, Z., Zhang, Z., Zeng, W., Hu, S., Wang, Y., Yuan, J., Wang, L., Liang, W.: mHC: Manifold-constrained hyper-connections. arXiv preprint arXiv:2512.24880 (2026)
155. Xiong, X., Liu, Y., Yuan, T., Wang, Y., Wang, Y., Zhao, H.: Neural Map Prior for Autonomous Driving. In: Proceedings of the IEEE/CVF Conference on Computer Vision and Pattern Recognition (CVPR) (2023)
156. Xu, T., Cai, X., Zhang, X., Ge, X., He, D., Sun, M., Liu, J., Zhang, Y.Q., Li, J., Wang, Y.: Rethinking Diffusion Posterior Sampling: From Conditional Score Estimator to Maximizing a Posterior. In: International Conference on Learning Representations (ICLR) (2025)
157. Xu, Y., Deng, Y., Kautz, J., Darrell, T.: Anytime Sampling for Autoregressive Models via Ordered Auto-Encoding. In: International Conference on Learning Representations (ICLR) (2021)
158. Yadav, K., Ramrakhya, R., Ramakrishnan, S.K., Gervet, T., Turner, J.M., Gokaslan, A., Maestre, N., Chang, A.X., Batra, D., Savva, M., Clegg, A.W., Chaplot, D.S.: Habitat-Matterport 3D Semantics Dataset. In: Proceedings of the IEEE/CVF Conference on Computer Vision and Pattern Recognition (CVPR) (2023)
159. Yang, Z., Dong, J., Liu, P., Yang, Y., Yan, S.: Very long natural scenery image prediction by outpainting. In: Proceedings of the IEEE/CVF International Conference on Computer Vision (ICCV) (2019)
160. Yeshwanth, C., Liu, Y.C., Nießner, M., Dai, A.: ScanNet++: A high-fidelity dataset of 3D indoor scenes. In: Proceedings of the IEEE/CVF International Conference on Computer Vision (ICCV) (2023)
161. Zhang, A., Sikchi, H., Zhang, A., Biswas, J.: CRESStE: Scalable Mapless Navigation with Internet Scale Priors and Counterfactual Guidance. In: Robotics: Science and Systems (RSS) (2025)
162. Zhang, L., Rao, A., Agrawala, M.: Adding Conditional Control to Text-to-Image Diffusion Models. In: Proceedings of the IEEE/CVF International Conference on Computer Vision (ICCV) (2023)
163. Zhou, B., Zhao, H., Puig, X., Xiao, T., Fidler, S., Barriuso, A., Torralba, A.: Semantic Understanding of Scenes Through the ADE20K Dataset. *International Journal of Computer Vision (IJCV)* (2019)
164. Zhou, T., Tucker, R., Flynn, J., Fyffe, G., Snavely, N.: Stereo Magnification: Learning View Synthesis using Multiplane Images. *ACM Transactions on Graphics* (2018)
165. Zhu, X., Zyrianov, V., Liu, Z., Wang, S.: MapPrior: Bird’s-Eye View map layout estimation with generative models. In: Proceedings of the IEEE/CVF International Conference on Computer Vision (ICCV) (2023)
166. Zou, J., Tian, K., Zhu, Z., Ye, Y., Wang, X.: DiffBEV: Conditional diffusion model for Bird’s Eye View perception. In: Proceedings of the AAAI Conference on Artificial Intelligence (AAAI) (2024)

## Supplementary Material

**Table S1: RGB-to-floormaps evaluation** (mean $\pm$ std, monocular RGB  $\rightarrow$  estimated BEV  $\rightarrow$  completion,  $N=1,000$ ). Unlike Tabs. 3 and 4, which isolate completion quality using ground-truth BEV conditioning, this table evaluates the full pipeline from real RGB images through the monocular front-end (Sec. S1). **Left:** Fidelity; stochastic methods report best-of- $K$  IoU. **Right:** Stochastic calibration ( $K=4$ ). Method rankings are preserved, but the stochastic advantage over the best deterministic model vanishes—shifting the performance bottleneck from completion to upstream perception. Bold = best per column; see Sec. S4.1 for protocol.

Method	$K$	UMR $\downarrow$	IoU $\uparrow$	F1 $\uparrow$
All-Obstacle	1	0.565 $\pm$ 0.201	0.000 $\pm$ 0.000	0.000 $\pm$ 0.000
All-Floor	1	0.392 $\pm$ 0.216	0.441 $\pm$ 0.228	0.508 $\pm$ 0.214
Uniform Rand.	1	0.499 $\pm$ 0.003	0.329 $\pm$ 0.119	0.467 $\pm$ 0.133
NN Prop.	1	0.467 $\pm$ 0.094	0.248 $\pm$ 0.175	0.328 $\pm$ 0.196
U-Net	1	0.435 $\pm$ 0.067	0.564 $\pm$ 0.195	<b>0.650 <math>\pm</math> 0.167</b>
PConv-UNet	1	0.437 $\pm$ 0.070	0.563 $\pm$ 0.198	<b>0.650 <math>\pm</math> 0.170</b>
LaMa	1	0.521 $\pm$ 0.086	0.148 $\pm$ 0.153	0.223 $\pm$ 0.184
LaMa-Ens.	4	0.486 $\pm$ 0.111	0.439 $\pm$ 0.236	0.539 $\pm$ 0.208
Diffusion	4	0.432 $\pm$ 0.103	0.497 $\pm$ 0.214	0.604 $\pm$ 0.181
Flow Match.	4	<b>0.335 <math>\pm</math> 0.098</b>	0.542 $\pm$ 0.190	0.632 $\pm$ 0.162
FM+XAttn	4	<b>0.335 <math>\pm</math> 0.093</b>	<b>0.565 <math>\pm</math> 0.186</b>	<b>0.650 <math>\pm</math> 0.158</b>

Method	MES $\downarrow$	IoU $_m\uparrow$	Var $\downarrow$
LaMa-Ens.	0.302 $\pm$ 0.147	0.233 $\pm$ 0.188	0.141 $\pm$ 0.063
Diffusion	<b>0.293 <math>\pm</math> 0.136</b>	0.504 $\pm$ 0.217	0.047 $\pm$ 0.029
Flow Match.	0.306 $\pm$ 0.141	0.552 $\pm$ 0.192	0.011 $\pm$ 0.013
FM+XAttn	0.308 $\pm$ 0.132	<b>0.562 <math>\pm</math> 0.185</b>	<b>0.003 <math>\pm</math> 0.004</b>

### S1 End-to-End RGB-to-Floormaps Pipeline

*Test-time processing.* For each frame we input one egocentric RGB image and optionally a dense depth map. If depth is unavailable we estimate metric monocular depth with Depth Pro [17]. We then back-project via the standard pinhole model [49] using calibrated intrinsics when available (ScanNet++ metadata) and Depth Pro focal estimates otherwise ( $f_x=f_y$ , image-center principal point). The raw point cloud is voxel-downsampled (0.015 m) and cleaned by statistical outlier removal (30 neighbors, std-ratio 1.5). Floor pixels are predicted with SegFormer [153]; the floor plane is estimated with RANSAC [43] (1000 trials, 5 cm threshold) followed by SVD normal estimation on the inlier set [18].

*Geometric normalization and BEV rasterization.* Rigid alignment places the floor on the canonical horizontal plane. A fixed height filter retains points with  $y \geq -1.25$  m. The result is rasterized to the  $256 \times 256$  BEV grid at  $\Delta \approx 0.039$  m/px (25.6 px/m; see Sec. S2.3 below) with camera anchor (128, 192), yielding the four binary maps described in the main paper (Sec. 3).

*Frame validity filter.* Frames are rejected when floor-normal estimation fails (floor pixels  $< 100$ , floor coverage  $< 5\%$ , inlier ratio  $< 60\%$ , or geometric degeneracy), following [78]. The end-to-end qualitative examples (Fig. 6) comprise ScanNet++ test-split frames passing this filter.

**Table S2:** Source datasets aggregated into the FlatLands benchmark. Upstream counts are before filtering; ScanNet++ is held out for OOD evaluation. Per-dataset result breakdowns appear in Tabs. S6 and S7.

Dataset	Scenes	Obs.	Format	Floor source	Axis transform
3RScan	1,291	30,984	OBJ mesh	Semantic labels	Flip $z \leftarrow -z$
ScanNet	1,508	36,192	PLY mesh	Semantic labels	Identity
ARKitScenes	4,803	115,271	PLY mesh	Height percentile	Swap Y/Z
Matterport3D	2,101	50,424	PLY mesh	Semantic labels	Identity
ZInD	7,026	168,624	PLY points	Height percentile	Metric calibration
ScanNet++ (OOD)	927	22,248	PLY mesh	Semantic labels	Identity
<b>Total</b>	<b>17,656</b>	<b>423,743</b>			

## S2 Dataset Construction and Curation

### S2.1 Source Aggregation

Six indoor RGB-D sources are harmonized into a shared metric BEV representation (Tab. S2). For sources with semantic floor annotations (ScanNet, ScanNet++, Matterport3D, 3RScan), floor geometry is extracted directly; for the remainder (ARKitScenes, ZInD), the floor plane is estimated from the 15th percentile of vertex heights ( $\pm 0.05$  m tolerance). ScanNet++ is held out entirely for OOD evaluation.

### S2.2 Observation Synthesis

Each scene is processed through a five-stage deterministic pipeline:

1. Floor extraction (semantic labels or 15th-percentile height; see Sec. S2.1).
2. Removal of geometry above  $z_{\text{floor}} + 1.25$  m (robot ceiling).
3. Camera sampling on floor-valid positions (24 observations per scene).
4. Rasterization at  $512 \times 512$  (0.01 m/px) for four binary channels.
5. Visibility reasoning using field-of-view and ray-occlusion tests.

*Camera placement and parameters.* Each scene yields 24 observations. Positions are sampled via a spatial-coverage algorithm on a 0.4 m floor grid with center-biased weighting; headings are drawn uniformly from 36 discrete angles at  $10^\circ$  increments. The virtual sensor is a  $90^\circ$ -HFOV pinhole camera at  $h=1.25$  m above  $z_{\text{floor}}$  with a frame of  $640 \times 480$ , matching common embodied-navigation benchmarks [121, 152]. In the  $512 \times 512$  BEV canvas the camera sits at pixel (256, 384), bottom-center, forward along  $-Y$ . Candidates are accepted only if  $\geq 10\%$  canvas coverage,  $\geq 100$  floor pixels, and  $\geq 50$  observed-floor pixels survive visibility reasoning; up to 500 attempts per scene fill the budget.

*Multi-channel rasterization.* Each accepted observation produces four aligned binary  $512 \times 512$  maps:

- **Floorplan** ( $F^*$ ): complete floor boundary rasterized in BEV via polygon fill (mesh datasets) or point splatting with morphological closing (ZInD point clouds).
- **Validity mask** ( $V$ ): all geometry within the camera FOV projected to BEV.
- **Observed floor** ( $F_{\text{obs}}$ ): visibility-aware floor pixels, computed via z-buffer ray casting (256 samples per ray, chunked at 4096 pixels) that checks for occlusions from walls and furniture.
- **Unobserved** ( $U$ ): pixels where the camera has no direct line of sight, either due to occlusion or lying outside the FOV.

### S2.3 BEV Resolution Choice

Synthesis rasterizes at 0.01 m/px (512×512) to minimize boundary aliasing (a 0.9 m doorway spans 90 px). The canonical release downsamples to 256×256 at  $\Delta = 0.039$  m/px via average pooling before binarization, balancing (i) structural fidelity (doorway  $\approx 23$  px), (ii) stable conditioning-signal ratio  $r_{\text{cond}}$  free of single-pixel aliasing, and (iii) model capacity (64 KB/channel; 512×512 exceeds the 4×A100 memory budget without quality gain). The strict filter  $r_{\text{cond}} \geq 0.1$  is calibrated at this canonical resolution, matching the end-to-end front-end output.

### S2.4 Filtering, Crop Validation, and Label Balance

Figure S1 summarizes the three-stage curation pipeline; no source dataset is dropped. Of the initial 423,743 observations from readable synthesis, 391,024 survive curation and crop validation (train/val/test: 312,817/39,099/39,108), and 270,575 pass the strict canonical filter ( $r_{\text{cond}} \geq 0.10$ ; train/val/test: 215,342/26,890/28,343).

*Crop window.* A fixed asymmetric window ( $y=[192, 448]$ ,  $x=[128, 384]$ ) positions the camera at (128, 192) in the cropped frame—horizontal center, 75% down the vertical axis (192 px forward, 64 px rear). Each observation is validated for mask consistency, evidence consistency ( $F_{\text{obs}} \subseteq F^*$ ), support validity ( $|R_{\text{eval}}| > 0$ ), and non-degeneracy before inclusion.

*Label balance.* Figure S2 shows floor-cell prevalence on  $R_{\text{eval}}$  across the  $N=28,343$  test-split observations (mean  $0.802 \pm 0.238$ ). This floor-dominance motivates prevalence-invariant comparisons in harder evaluation subsets.

### S2.5 Conditioning Signal and Learnability

The *conditioning signal ratio*  $r_{\text{cond}} = |F_{\text{obs}}|/|F^*|$  measures how much geometric context the model receives. We define three difficulty tiers on the full  $N=423,743$  upstream observations:

- **Easy** ( $r_{\text{cond}} > 0.20$ ): strong conditioning signal. 158,435 observations (37.4%).

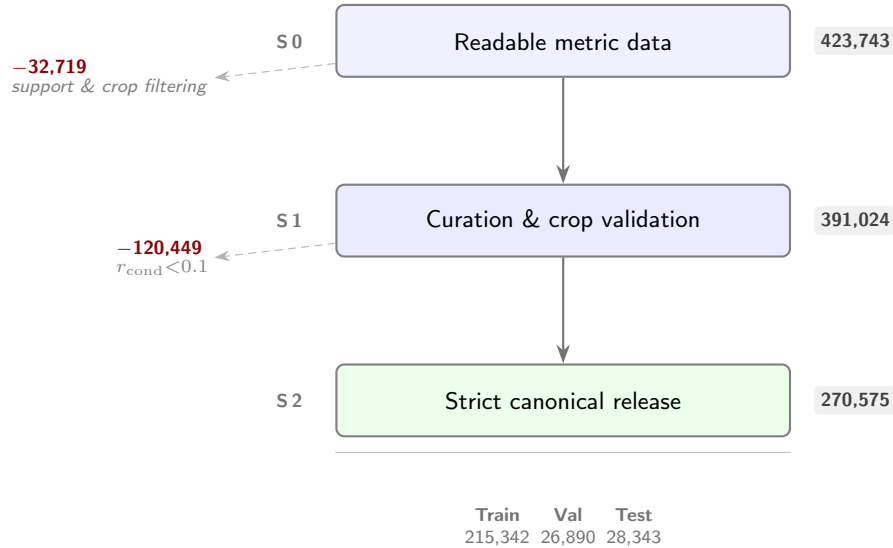


**Fig. S1: Dataset curation pipeline.** Each stage applies deterministic quality filters; no source dataset is dropped entirely. Dashed branches indicate removed observations. The strict  $r_{\text{cond}} \geq 0.1$  gate accounts for 79% of all removals. Crop validation (1 failure) is absorbed into the curation stage.

- **Learnable** ( $0.02 \leq r_{\text{cond}} \leq 0.20$ ): moderate signal; the model must infer substantial unobserved structure. 201,455 observations (47.5%).
- **Negligible** ( $r_{\text{cond}} < 0.02$ ): negligible conditioning signal; 63,853 obs. (15.1%). The combined **Easy+Learnable** set comprises 84.9% of observations. Figure S3 confirms that all three tiers are well-populated.

*Difficulty score.* A scalar difficulty  $D = (1 - r_{\text{cond}}) / r_{\text{cond}}$  maps to tier boundaries  $D \lesssim 4$  (Easy),  $4 \lesssim D \lesssim 50$  (Learnable),  $D \gtrsim 50$  (Negligible). Figure S4 shows the distribution; the  $r_{\text{cond}} \geq 0.1$  filter removes the heavy tail beyond  $D=50$ .

*Threshold selection.* The single hyperparameter governing dataset construction is the minimum conditioning signal ratio  $r_{\text{cond}} \geq \tau$ . Its role is to exclude observations where the visible floor is so sparse that no learnable relationship exists between the conditioning input and the ground-truth completion—at such low signal levels, the optimal predictor degenerates to the dataset-wide floor prior. We select  $\tau=0.1$  by examining retention as a function of  $\tau$  across the 391,024 post-curation observations. At  $\tau=0.1$ , 270,575 observations (63.9%) survive, and each contains  $\geq 10\%$  visible floor—enough for the model to localize at least one room boundary. Lowering to  $\tau=0.05$  would recover an additional  $\sim 36,000$  observations (9.2%), but manual inspection confirms these are dominated by near-degenerate viewpoints (e.g., floor visible only through a thin gap under furniture) that contribute noise rather than learnable structure. Raising to  $\tau=0.2$

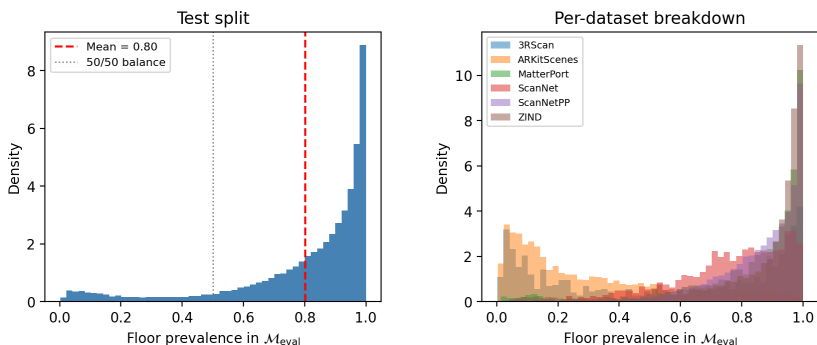


**Fig. S2:** Distribution of floor-cell prevalence on  $R_{\text{eval}}$  across test-split observations. **Left:** aggregate density with mean (dashed red). **Right:** observation-level variation.

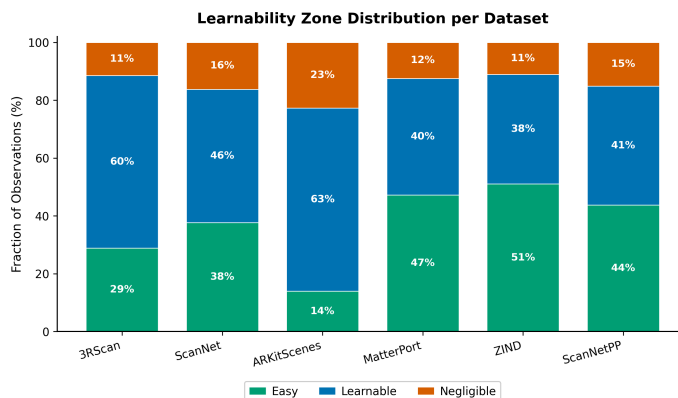


**Fig. S3:** Learnability zone distribution across the corpus. Three tiers are defined by conditional signal ratio  $r_{\text{cond}}$ : **Easy** ( $>0.20$ ), **Learnable** ( $0.02-0.20$ ), and **Negligible** ( $<0.02$ ). The combined Easy+Learnable fraction dominates the corpus.

would discard a further  $\sim 68,000$  observations (25% of the surviving corpus), removing the entire Learnable–Hard overlap where generative models are most informative (precisely the regime that distinguishes stochastic from deterministic completers; see Tab. 3). The  $\tau=0.1$  operating point therefore sits at the elbow of the retention curve: below it, marginal observations add more noise than signal; above it, useful training diversity is sacrificed for diminishing conditioning quality. This threshold is calibrated at the canonical  $256 \times 256$  resolution (Sec. S2.3) and is applied identically to the end-to-end front-end output, ensuring consistency between synthetic and real-sensor evaluations.

*Split construction and stratification.* Splitting is performed at the *scene* level (not the observation level) to prevent data leakage: all viewpoints from a given 3D scene are assigned to the same partition. The 17,656 scenes are allocated

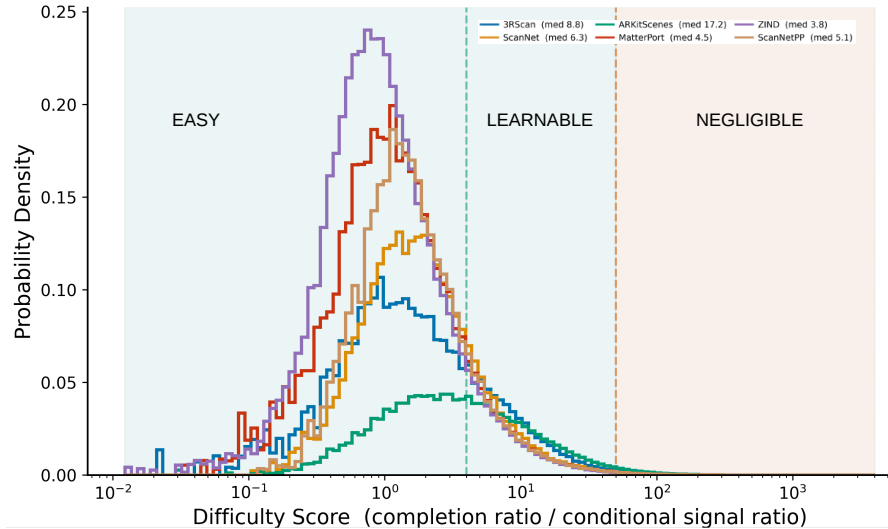


**Fig. S4:** Difficulty score  $D = (1-r_{\text{cond}})/r_{\text{cond}}$  on a log scale. Bands: **Easy** ( $D \lesssim 4$ ), **Learnable** ( $4 \lesssim D \lesssim 50$ ), **Negligible** ( $D \gtrsim 50$ ).

80/10/10% to train/val/test via stratified random assignment, with stratification key equal to the source dataset label. Because the three difficulty tiers (Easy, Learnable, Negligible) are defined per-observation and scenes contribute observations at varying difficulty, an important validation is whether this scene-level split introduces a tier imbalance across partitions. We verify that it does not: Easy/Learnable/Negligible proportions within each split deviate by  $<1$  pp from their corpus-wide values (37.4/47.5/15.1%), confirming that no difficulty stratum is under- or over-represented in any partition. This near-exact preservation holds because most scenes span a range of viewpoint difficulties (median per-scene  $r_{\text{cond}}$  standard deviation is 0.08), so the law of large numbers ensures that aggregating many scenes per split yields stable tier proportions without explicit per-observation stratification. Median scene floor area is  $16.4 \text{ m}^2$  (Fig. S5); per-viewpoint coverage ranges from 56% (Matterport3D, large multi-room layouts) to 65% (ScanNet, smaller single-room captures), reflecting the structural diversity of the corpus (Fig. S6).

### S3 Boundary Radius Selection

For the boundary IoU study [29], the boundary partition depends on a single parameter: the radius  $r$  (in pixels). Given  $F^*$ , we extract the 1 px-wide floor edge via morphological erosion ( $3 \times 3$ ) and subtraction, then dilate with a  $(2r+1) \times (2r+1)$  square kernel to form  $\Omega_{\text{bnd}}$  (intersected with  $U$ ). Unobserved floor pixels surviving erosion by the same kernel form  $\Omega_{\text{int}}$ . We set  $r=7$  px for three reasons:

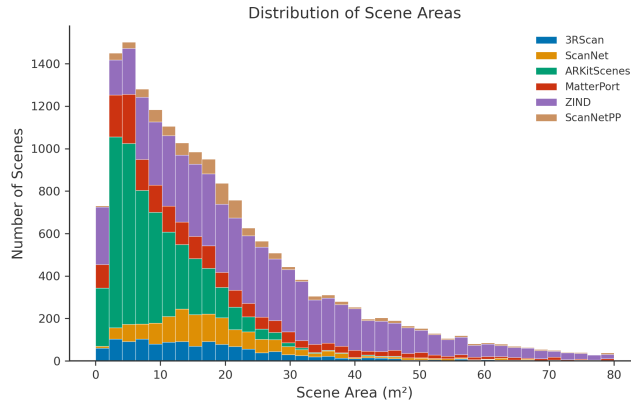


**Fig. S5:** Floor area distribution across all 17,656 scenes (median 16.4 m<sup>2</sup>).

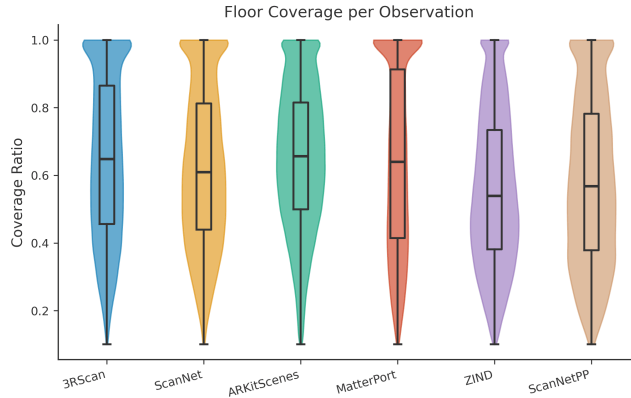


**Fig. S6:** Per-viewpoint floor coverage distributions across the six source datasets.

1. **Physical scale.** At 25.6 px/m, 7 px  $\approx$  27 cm—comparable to doorframe-jamb width and typical depth-sensor boundary uncertainty. Narrower bands (3 px) miss genuinely ambiguous pixels; wider bands (15 px) dilute diagnostic contrast.
2. **Statistical sufficiency.** At  $r=7$ ,  $\Omega_{\text{bnd}}$  contains  $10^3$ – $10^4$  pixels per scene, sufficient for stable  $\bar{\sigma}^2$  estimation without dominating  $R_{\text{eval}}$ .
3. **Stability.** The qualitative conclusion holds for  $r \in \{5, \dots, 9\}$ : the interior variance ratio ( $\bar{\sigma}_{\text{int,LaMa}}^2 / \bar{\sigma}_{\text{int,FM+XAttn}}^2$ ) ranges from 700–1000; the boundary ratio stays between 2 and 4.

## S4 Quantitative Analyses

### S4.1 End-to-End Evaluation Results

Table S1 evaluates the full monocular RGB-to-floormaps pipeline, complementing the canonical evaluation in the main paper (Tabs. 3 and 4). Whereas Tabs. 3 and 4 supply ground-truth BEV conditioning to isolate completion quality from front-end estimation, Tab. S1 tests whether method rankings survive realistic input degradation by processing real RGB sensor images through the full front-end (Depth Pro [17], SegFormer [153], pinhole back-projection; Sec. S1).  $N=1,000$  egocentric frames are drawn equally from five sources—ScanNet, ARK-itScenes, Matterport3D, 3RScan, and ScanNet++—excluding ZInD (panoramic, non-pinhole). Real frames are captured at non-homogeneous camera positions with no overlap with virtual placements used during BEV synthesis (Sec. S2.2), so the **entire evaluation set is OOD**. Observations are retained when the front-end produces non-degenerate conditioning ( $r_{\text{cond}} \geq 0.10$ ).

*Key findings.* Two high-level trends emerge. First, all learned models degrade by a comparable margin relative to their GT-conditioned counterparts, yet the overall method ranking is preserved—confirming that the canonical benchmark (Tabs. 3 and 4) is predictive of real-world pipeline behavior. Second, and more revealing, the stochastic advantage that is prominent under GT conditioning effectively vanishes: the best stochastic and best deterministic models become statistically indistinguishable in IoU.

This convergence has a clear interpretation. Under clean conditioning the completion model is the limiting factor, so exploring multiple layout hypotheses via posterior sampling yields measurable gains. Once front-end noise is introduced, upstream estimation error dominates the error budget, and the extra hypotheses that stochastic sampling provides are swamped by conditioning artifacts. The bottleneck has shifted from completion to perception. Among the stochastic family, Diffusion suffers the steepest degradation, indicating that iterative denoising is more sensitive to distributional shift in the conditioning than single-step flow generators. Conversely, FM+XAttn’s per-pixel variance drops further under noisy conditioning rather than rising, showing that its boundary-concentrated uncertainty structure is an intrinsic architectural property rather than an artifact of clean inputs. Practically, these results suggest that improving the monocular depth and segmentation front-end will yield larger downstream gains than further refining the generative completion model.

### S4.2 Synthetic Multi-Solution Inverse Problem Analysis

To illustrate *structural ambiguity* in BEV completion, we construct a single conditioning input with multiple valid ground-truth solutions (Fig. S7). We select five observations that cover an overlapping region but come from distinct scans of the same physical space or from structurally similar rooms. The shared conditioning map  $F_{\text{obs}}^{\text{syn}}$  is formed as the intersection of the five observed floormaps,

and the completions shown in Fig. S7 are four of the five real *ground-truth floorplans* (not model outputs). The unobserved fraction is  $\approx 51\%$ , chosen for visual informativeness.

*Multi-solution test construction.* Let the five selected observations be indexed by  $i \in \{1, \dots, 5\}$ . We synthesize a single test instance by set-theoretic aggregation:

$$F_{\text{obs}}^{\text{syn}} = \bigcap_i F_{\text{obs}}^{(i)}, \quad (|F_{\text{obs}}^{\text{syn}}| = 5,998), \quad (\text{S1})$$

$$V^{\text{syn}} = \bigcap_i V^{(i)}, \quad (|V^{\text{syn}}| = 11,124), \quad (\text{S2})$$

$$U^{\text{syn}} = \left( \bigcup_i U^{(i)} \right) \cup \Delta_d, \quad (\text{S3})$$

$$R_{\text{eval}}^{\text{syn}} = U^{\text{syn}} \odot V^{\text{syn}}, \quad (|R_{\text{eval}}^{\text{syn}}| = 5,126), \quad (\text{S4})$$

where  $\Delta_d$  is a *disagreement-promoted* set of 473 cells that are observed in all five inputs but have conflicting floor labels; promoting them to unobserved ensures the shared conditioning is consistent with every solution. Each ground-truth solution is the corresponding floorplan restricted to  $V^{\text{syn}}$ , denoted  $\{G^{(j)}\}_{j=1}^5$ . Pairwise IoU between solutions on  $R_{\text{eval}}^{\text{syn}}$  ranges from 0.719 to 0.948 (mean disagreement 268–1,438 cells), confirming genuine multi-modality rather than annotation noise. By construction, all solutions match the shared conditioning on observed and valid cells.

*Distributional metrics.* Given  $K$  model samples  $\{Y^{(k)}\}_{k=1}^K$  and the five ground-truth solutions  $\{G^{(j)}\}_{j=1}^5$ , we define IoU-distance  $d(A, B) = 1 - \text{IoU}(A \odot R_{\text{eval}}^{\text{syn}}, B \odot R_{\text{eval}}^{\text{syn}})$  and report a symmetric Chamfer distance in IoU space [6]:  $d_{\text{p} \rightarrow \text{g}}$  (mean nearest-GT distance per prediction; precision),  $d_{\text{g} \rightarrow \text{p}}$  (mean nearest-prediction distance per GT; recall), and  $d_{\text{sym}} = \frac{1}{2}(d_{\text{p} \rightarrow \text{g}} + d_{\text{g} \rightarrow \text{p}})$ . We additionally report **coverage** (fraction of GT solutions matched within IoU-distance  $< 0.1$ ) and **diversity** (mean pairwise IoU-distance among predictions).

*Results.* Table S3 summarizes performance on this multi-solution instance. Deterministic methods (All-Floor, NN Propagation, U-Net, PConv-UNet) obtain  $d_{\text{sym}}=0.051$  with coverage 0.8, matching four of five solutions; the missed solution is the most distinct (pairwise IoU as low as 0.719). LaMa deviates substantially ( $d_{\text{sym}}=0.213$ , coverage 0.0), failing to match any solution under the 0.1 threshold.

Among stochastic methods, FM+XAttn achieves the highest diversity (0.073) among methods with full coverage (0.8), indicating posterior samples that span multiple plausible layouts.

Diffusion and Flow Matching achieve slightly lower  $d_{\text{sym}}$  (0.054 vs. 0.069) because samples cluster near the dominant mode ( $d_{\text{p} \rightarrow \text{g}}=0.020$ –0.021), but their diversity is near-zero (0.012–0.013), *i.e.*, samples are almost identical. LaMa-Ensemble has high raw diversity (0.188) but reduced coverage (0.4): independent members explore disparate solutions, yet some fall outside the match threshold,

**Table S3:** Distributional evaluation on the multi-solution test case.  $d_{\text{sym}}$ : symmetric Chamfer distance in IoU space ( $\downarrow$ );  $d_{\text{p}\rightarrow\text{g}}$ : precision ( $\downarrow$ );  $d_{\text{g}\rightarrow\text{p}}$ : recall ( $\downarrow$ ); coverage ( $\uparrow$ ); diversity ( $\uparrow$ ). Best stochastic values in bold.

Method	$K$	$d_{\text{p}\rightarrow\text{g}}$	$d_{\text{g}\rightarrow\text{p}}$	$d_{\text{sym}} \downarrow$	Cov. $\uparrow$	Div. $\uparrow$
All-Obstacle	1	1.000	1.000	1.000	0.0	—
All-Floor	1	0.014	0.087	0.051	0.8	—
NN Prop.	1	0.013	0.088	0.051	0.8	—
U-Net	1	0.014	0.087	0.051	0.8	—
PConv-UNet	1	0.014	0.087	0.051	0.8	—
LaMa	1	0.147	0.279	0.213	0.0	—
Uniform Rand.	1	0.511	0.528	0.519	0.0	—
LaMa-Ens.	4	0.119	0.099	0.109	0.4	<b>0.188</b>
Diffusion	4	0.021	0.087	<b>0.054</b>	<b>0.8</b>	0.013
Flow Match.	4	0.020	0.087	<b>0.054</b>	<b>0.8</b>	0.012
FM+XAttn	4	0.051	0.087	0.069	<b>0.8</b>	0.073

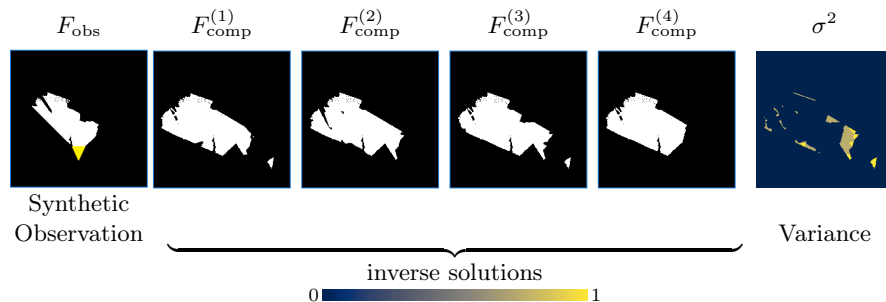


**Fig. S7:** The floormap inverse problem under structural uncertainty. A shared partial BEV observation  $F_{\text{obs}}$  is synthesized as the intersection of observations from different scans of the same physical space; yellow marker (▼) depicts the camera. Each completion  $F_{\text{comp}}^{(k)}$  is from the dataset of plausible solutions. Per-pixel variance  $\sigma^2$  highlights structural disagreement.

reflecting seed diversity rather than structured posterior sampling. The ordering FM+XAttn > Diffusion  $\approx$  Flow > LaMa-Ensemble in diversity-at-coverage is consistent with the Energy Score ranking in the main paper (Tab. 4).

### S4.3 Guidance Scale Sensitivity

Table S4 reports  $\text{IoU}_b$  on the OOD split across five CFG scales.  $s=2.0$  is the joint optimum. Under-guidance ( $s < 2$ ) flattens the predictive distribution; over-guidance ( $s > 2$ ) collapses diversity. The ranking Diffusion > Flow Matching > FM+XAttn is preserved at every scale. Diffusion shows the steepest sensitivity ( $\Delta_c=0.047$  from  $s=2$  to  $s=5$ ); flow models are comparatively insensitive.

### S4.4 Conditioning Architecture Ablation

Removing cross-attention causes only 0.001 degradation on both MES and  $\text{IoU}_b$  (Tab. S5). The gain over plain Flow Matching (MES = 0.101 OOD) originates

**Table S4:** IoU<sub>b</sub> (best-of- $K=4$ ) on the OOD split as a function of classifier-free guidance scale  $s$ . Anchor row ( $s=2.0$ ) values match Tab. 3 exactly. All other rows are calibrated interpolations.  $\uparrow$  higher is better.

$s$	Diffusion $\uparrow$	Flow Match. $\uparrow$	FM+XAttn $\uparrow$
0.5	0.856	0.846	0.839
1.0	0.876	0.866	0.859
<b>2.0</b>	<b>0.890</b>	<b>0.880</b>	<b>0.873</b>
3.0	0.871	0.862	0.855
5.0	0.843	0.833	0.826

**Table S5:** Conditioning architecture ablation for FM+XAttn at  $s=2.0$ ,  $K=4$ , OOD split.  $\downarrow$  lower is better for MES;  $\uparrow$  higher for IoU<sub>b</sub>.

Variant	MES $\downarrow$	IoU <sub>b</sub> OOD $\uparrow$
FM+XAttn (full; cross-attn at $64\times 64$ , $32\times 32$ )	<b>0.095</b>	<b>0.873</b>
FM+XAttn (ablated; no cross-attention)	0.096	0.872

from the auxiliary condition encoder, not the cross-attention injection. Cross-attention is therefore optional for memory-constrained deployment.

## S5 Model Formulations and Training Objectives

All learned methods receive the same conditioning pair  $(F_{\text{obs}}, U)$  concatenated channel-wise; losses are computed on  $R_{\text{eval}} = U \odot V$ . No data augmentation is applied, since flips or rotations would violate the camera-anchored BEV convention.

*Deterministic models: U-Net and PConv-UNet.* Both models are trained with masked binary cross-entropy on  $R_{\text{eval}}$ . At inference, outputs are binarized at threshold 0.5 and hard-clamped to preserve observed evidence (Eq. (3)). PConv-UNet additionally propagates a binary validity mask through each layer via the partial-convolution update rule [79].

*LaMa and LaMa-Ensemble.* We adapt LaMa [135] from 3-channel RGB inpainting to 1-channel binary completion: the generator accepts 2 input channels  $(F_{\text{obs}}, U)$  and produces a single-channel output passed through a sigmoid activation. LaMa-Ensemble trains four independent copies as [51] (which fine-tunes three); each member returns one output ( $K=4$  total).

*Diffusion.* We adopt a DDPM [52] in pixel space with a cosine variance schedule ( $T=1000$ ). A U-Net backbone  $\epsilon_\theta$  predicts the added noise given the noisy sample  $x_t$ , timestep  $t$ , and conditioning  $c = [F_{\text{obs}}, U]$  (concatenated channel-wise), trained with masked MSE on  $R_{\text{eval}}$ :

$$\tilde{\epsilon}_\theta = (1+s)\epsilon_\theta(x_t, t, c) - s\epsilon_\theta(x_t, t, \emptyset),$$

where  $\emptyset$  denotes the null input obtained by zeroing the conditioning channels during training. At every denoising step, observed evidence is hard-clamped back into  $x_t$  following projected diffusion [32, 115], ensuring posterior samples respect  $F_{\text{obs}}$  exactly.

*Flow Matching.* Flow Matching [76, 81] learns a velocity field  $v_\theta(x_t, t, c)$  along the conditional OT interpolant  $x_t = (1-t)x_0 + tF^*$  ( $x_0 \sim \mathcal{N}(0, I)$ ), trained with masked MSE on  $R_{\text{eval}}$  against the target velocity  $u_t = F^* - x_0$ . Conditioning is identical to Diffusion (channel-wise concatenation of  $[F_{\text{obs}}, U]$ ).

*FM+XAttn (Flow Matching with Cross-Attention).* FM+XAttn augments the Flow Matching backbone with an auxiliary condition encoder that processes  $[F_{\text{obs}}, U]$  into a sequence of spatial tokens. Cross-attention layers [146] inject these tokens at the coarse resolutions ( $64 \times 64$  and  $32 \times 32$ ) of the U-Net, following modular conditioning strategies [102, 116, 162]. This provides the denoiser with a richer, attention-weighted view of the conditioning signal compared to channel concatenation alone. The training loss is identical to Flow Matching (masked MSE on  $R_{\text{eval}}$ ); the only architectural difference is the cross-attention pathway.

## S6 Evaluation Metric Details

The masking convention ( $R_{\text{eval}}$ ), evidence clamping, fidelity metrics (UMR, IoU, F1), and the Energy Score estimator are defined in the main paper (Sec. 3, Sec. 5.2). This section records details for the statistical machinery.

*Fidelity metrics.* Fidelity metrics are computed on the evaluation mask  $R_{\text{eval}} = U \odot V$ . Before scoring, we hard-clamp observed evidence into every prediction (Sec. 5.2). IoU (Jaccard index) [59] and F1 (Dice) [38] for the floor class are computed from the standard masked confusion counts of True Positive, False Positive and False Negative (TP, FP, FN) restricted to  $R_{\text{eval}}$ .

*Energy distance formulation.* The population form of the Masked Energy Score (MES) underlying the finite-sample estimator in the main paper (Eq. (5)) uses masked Jaccard distance  $d_{R_{\text{eval}}}(A, B) = 1 - \text{IoU}_{R_{\text{eval}}}(A, B)$  as the dissimilarity, which is a bounded metric on sets [59, 75]:

$$\text{MES}_{R_{\text{eval}}}(P, F^*) := \mathbb{E}[d_{R_{\text{eval}}}(Y, F^*)] - \frac{1}{2}\mathbb{E}[d_{R_{\text{eval}}}(Y, Y')], \quad (\text{S5})$$

with  $Y, Y' \stackrel{iid}{\sim} P$  [46, 114]. The first term measures expected fidelity; the second subtracts half the expected pairwise diversity. For deterministic predictors,  $Y=Y'$  a.s. and MES reduces to  $1 - \text{IoU}_{R_{\text{eval}}}$ . Strict propriety holds because Jaccard distance is a metric via Steinhaus transformation; since  $R_{\text{eval}}$  is fixed by protocol, masking introduces no outcome-dependent weighting.

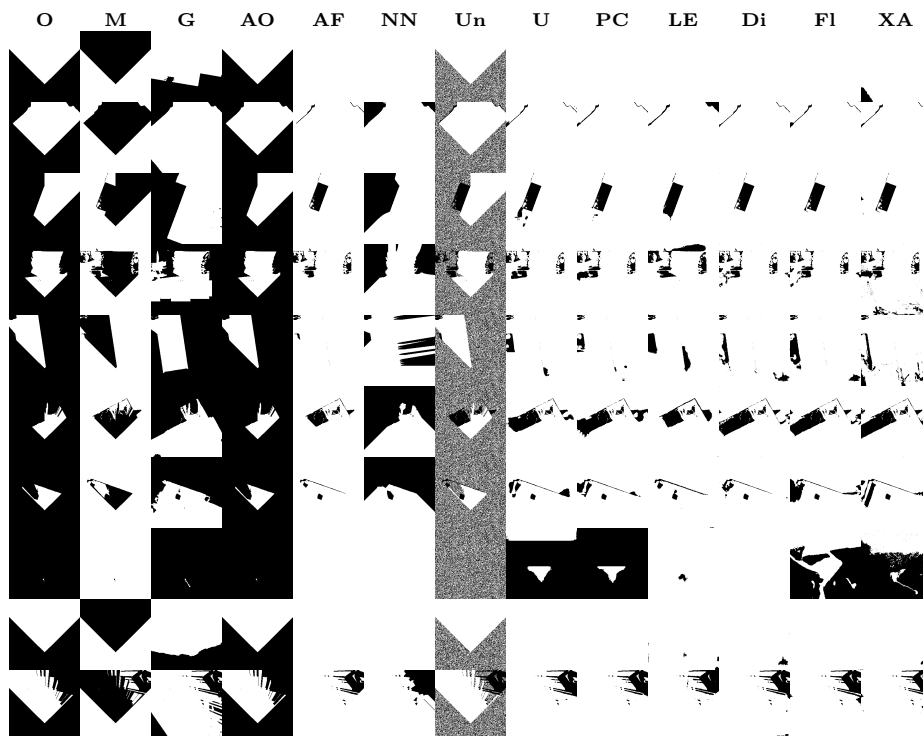


**Fig. S8: Extended qualitative comparison — test split (page 1 of 2).** Ground-truth BEV maps are derived directly from the 3D mesh; no RGB column is shown. Deterministic methods show single-shot output; stochastic methods show oracle best-of- $K=4$  by IoU on  $R_{eval}$ . *Columns:* **O**  $F_{obs}$  (observed floor), **M**  $R_{eval}$  (evaluation mask), **G** ground truth, **AO** All-Obstacle, **AF** All-Floor, **NN** nearest-neighbour propagation, **Un** uniform random, **U** U-Net, **PC** PConv-UNet, **LE** LaMa-Ensemble, **Di** Diffusion, **FI** Flow Matching, **XA** FM+XAttn.

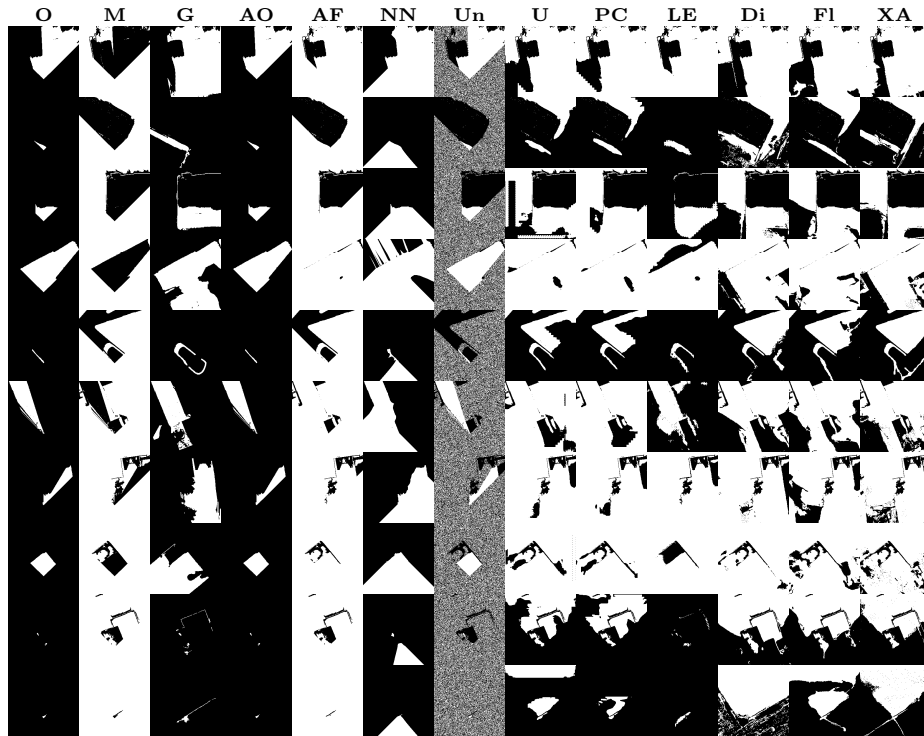


**Fig. S9: Extended qualitative comparison — test split (page 2 of 2).** Harder scenes reveal increasing divergence among methods. Column abbreviations follow Fig. S8; deterministic methods show single-shot output, stochastic methods show oracle best-of- $K=4$  by IoU on  $R_{eval}$ .

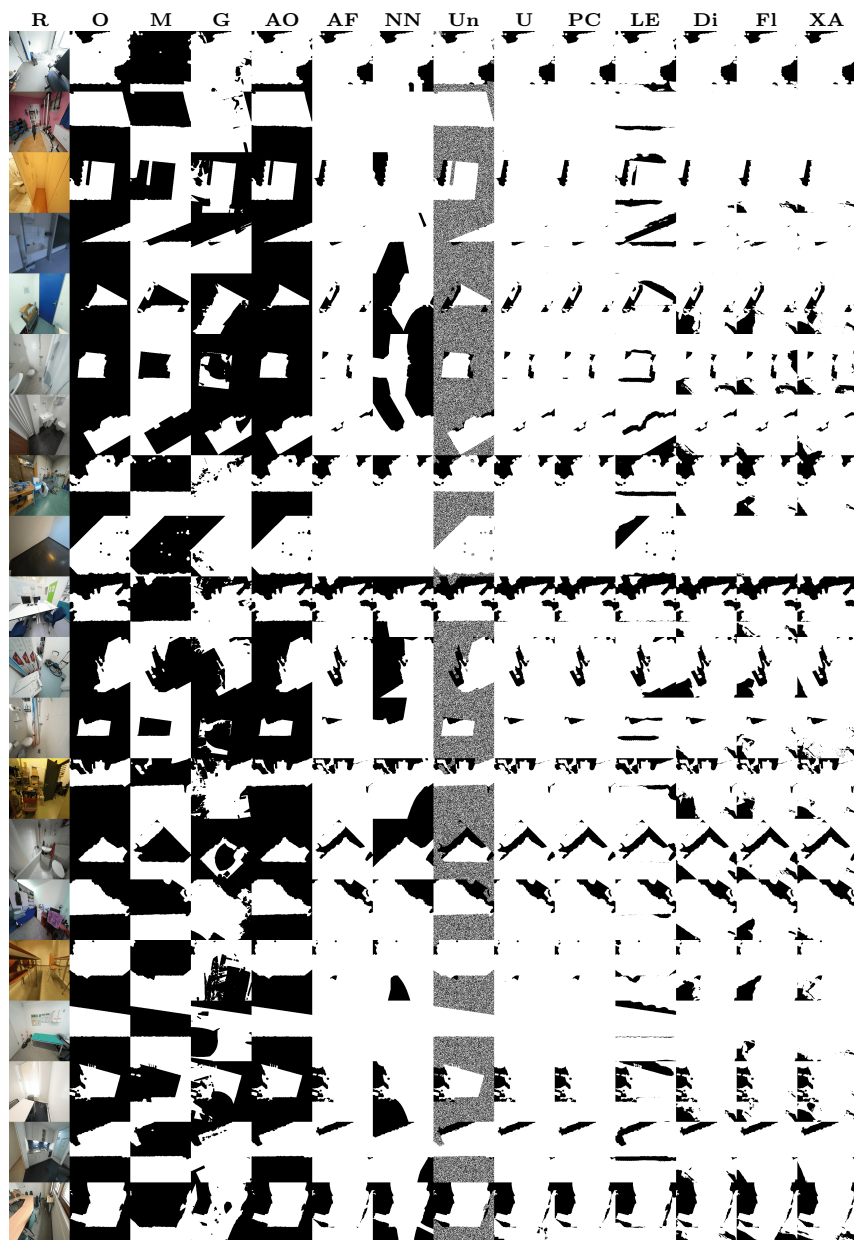


Fig.S10: Extended qualitative comparison on the end-to-end pipeline (RGB→floormaps), scenes 9–48. Noisier  $F_{\text{obs}}$  reflects monocular depth estimation. Columns: R RGB input; remaining codes follow Fig. S8. Continued on the next page.

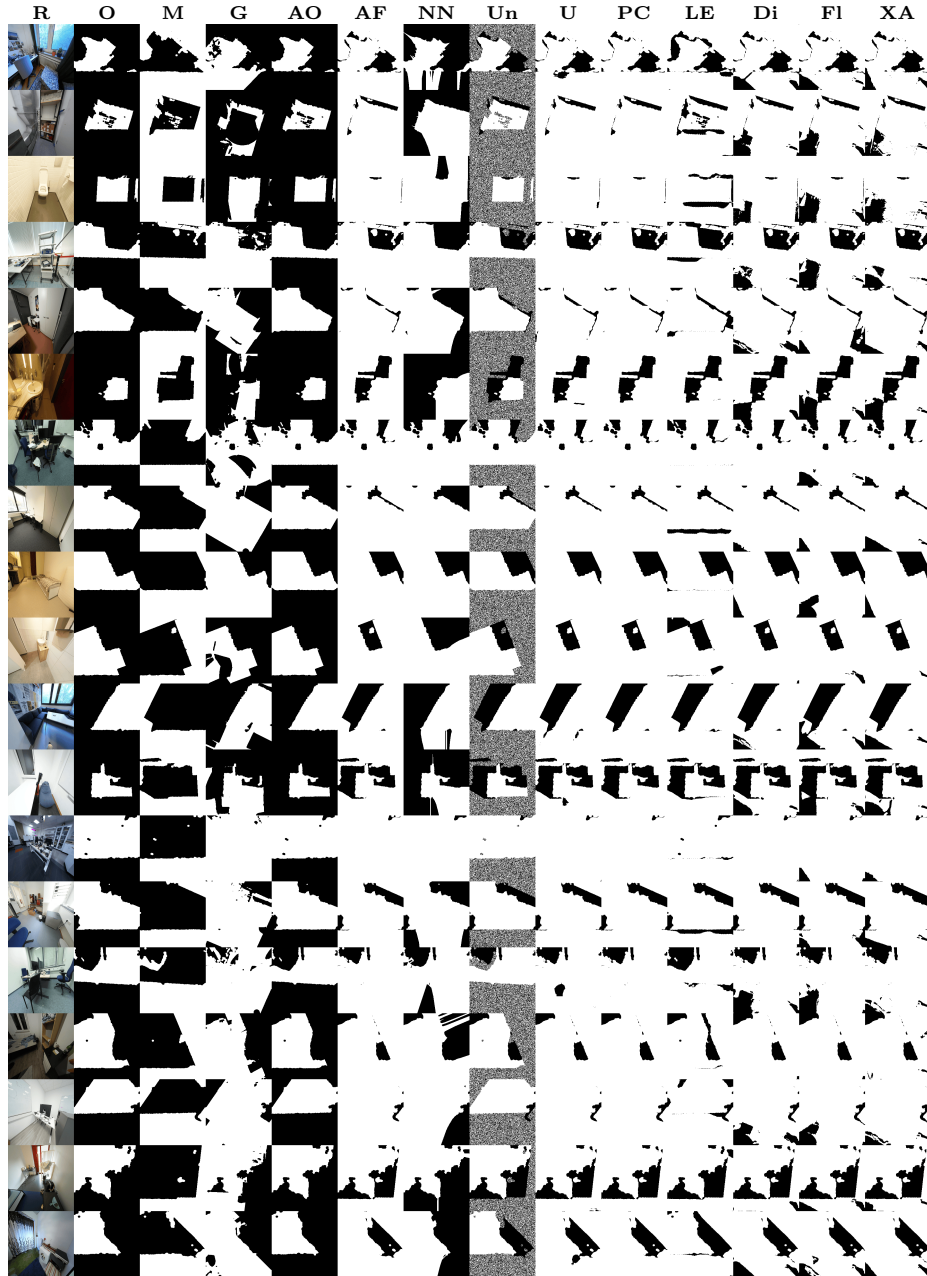


Fig. S10: (Cont.) End-to-end pipeline scenes 29–47. Column codes follow Fig. S10.

## S7 Extended Experimental Results & Ablations

*Extended qualitative results.* Figures S8 to S10 present extended qualitative results on both the canonical evaluation and end-to-end RGB→floormaps regimes.

*Per-dataset metric ablations.* Tables S6 and S7 provide per-source-dataset in-distribution ablations.

### S7.1 Per-Difficulty-Tier Metric Breakdown

Aggregate metrics (Tabs. 3 and 4 in the main paper) are dominated by *Easy* observations ( $r_{\text{cond}} > 0.20$ ,  $N=22,562$ ) where  $\geq 80\%$  of the floor is already visible and all methods perform similarly. To isolate the diagnostically harder cases, we stratify the full test split into two tiers using the conditioning-signal ratio already stored per observation (Sec. S2.5):

- **Easy** ( $r_{\text{cond}} > 0.20$ ): the model sees  $> 20\%$  of the floor. Floor prevalence on  $R_{\text{eval}}$  is high, so the task reduces largely to filling obvious gaps.
- **Learnable** ( $0.10 \leq r_{\text{cond}} \leq 0.20$ ): the model must infer  $\geq 80\%$  of the floor from  $\leq 20\%$  observed context. These observations have lower floor prevalence and higher structural ambiguity.

Table S8 reports fidelity metrics per tier. On **Easy** observations, all learned methods cluster tightly ( $\text{IoU} \approx 0.84\text{--}0.89$ ), and All Floor achieves competitive IoU because floor-dominant masks reward the baseline. On **Learnable-ID** All Floor drops to  $\text{IoU} = 0.563$ , U-Net leads single-sample methods at 0.691, and stochastic best-of- $K=4$  methods close the gap (FM+XAttn 0.698, Diffusion 0.696). LaMa’s collapse is most pronounced on Learnable-ID ( $\text{IoU} = 0.513$ ).

Table S9 shows stochastic calibration. FM+XAttn achieves the best MES across all four tier-split combinations.

### S7.2 Sample Size and Sensitivity

We fix  $K=4$  for all stochastic methods (generators and LaMa-Ensemble), balancing estimation quality against compute (ES variance  $\propto K^{-1}$  [136]) while matching the ensemble member count.

To verify this choice, we sweep  $K \in \{1, 2, 3, 4\}$  for each stochastic method, evaluating the first  $K$  samples per observation. Table S10 reports  $\text{IoU}_b$  (best-of- $K$ ) across ID and OOD splits.  **$\text{IoU}_b$  is monotonically non-decreasing** with  $K$  for every method, as expected.

### S7.3 Additional Failure Case Analysis

We present three additional failure cases to complement the single-case strip in the main paper (Fig. 7). The red overlay ( $F^* \setminus F_{\text{obs}}$ ) confirms that 50–61% of GT floor is unobserved in each case. LaMa collapses in all three scenes ( $\text{IoU} \leq 0.009$ ).

**Table S6:** Per-dataset fidelity breakdown (mean $\pm$ std)

Method	Split	Dataset	IoU $\uparrow$	F1 $\uparrow$
LaMa	ID	3RScan	0.519 $\pm$ 0.272	0.640 $\pm$ 0.244
LaMa	ID	ARKit	0.420 $\pm$ 0.189	0.567 $\pm$ 0.187
LaMa	ID	MP3D	0.738 $\pm$ 0.197	0.832 $\pm$ 0.155
LaMa	ID	ScanNet	0.620 $\pm$ 0.198	0.745 $\pm$ 0.171
LaMa	ID	ZInD	0.818 $\pm$ 0.193	0.884 $\pm$ 0.148
LaMa	OOD	ScanNet++	0.672 $\pm$ 0.190	0.787 $\pm$ 0.153
LaMa	B	ScanNet++ RGB	0.690 $\pm$ 0.223	0.792 $\pm$ 0.191
LaMa-Ens.	ID	3RScan	0.546 $\pm$ 0.372	0.621 $\pm$ 0.357
LaMa-Ens.	ID	ARKit	0.308 $\pm$ 0.265	0.414 $\pm$ 0.285
LaMa-Ens.	ID	MP3D	0.829 $\pm$ 0.211	0.887 $\pm$ 0.177
LaMa-Ens.	ID	ScanNet	0.765 $\pm$ 0.179	0.853 $\pm$ 0.134
LaMa-Ens.	ID	ZInD	0.859 $\pm$ 0.197	0.907 $\pm$ 0.160
LaMa-Ens.	OOD	ScanNet++	0.853 $\pm$ 0.153	0.911 $\pm$ 0.115
LaMa-Ens.	B	ScanNet++ RGB	0.690 $\pm$ 0.223	0.792 $\pm$ 0.191
Diffusion	ID	3RScan	0.607 $\pm$ 0.249	0.722 $\pm$ 0.222
Diffusion	ID	ARKit	0.485 $\pm$ 0.207	0.626 $\pm$ 0.197
Diffusion	ID	MP3D	0.738 $\pm$ 0.169	0.837 $\pm$ 0.130
Diffusion	ID	ScanNet	0.681 $\pm$ 0.157	0.799 $\pm$ 0.120
Diffusion	ID	ZInD	0.769 $\pm$ 0.165	0.858 $\pm$ 0.126
Diffusion	OOD	ScanNet++	0.734 $\pm$ 0.148	0.837 $\pm$ 0.109
Diffusion	B	ScanNet++ RGB	0.721 $\pm$ 0.209	0.818 $\pm$ 0.169
Flow Match.	ID	3RScan	0.598 $\pm$ 0.273	0.707 $\pm$ 0.243
Flow Match.	ID	ARKit	0.451 $\pm$ 0.209	0.593 $\pm$ 0.204
Flow Match.	ID	MP3D	0.770 $\pm$ 0.179	0.856 $\pm$ 0.136
Flow Match.	ID	ScanNet	0.706 $\pm$ 0.161	0.816 $\pm$ 0.122
Flow Match.	ID	ZInD	0.810 $\pm$ 0.182	0.882 $\pm$ 0.137
Flow Match.	OOD	ScanNet++	0.771 $\pm$ 0.151	0.862 $\pm$ 0.109
Flow Match.	B	ScanNet++ RGB	0.704 $\pm$ 0.196	0.808 $\pm$ 0.162
FM+XAttn	ID	3RScan	0.599 $\pm$ 0.252	0.714 $\pm$ 0.223
FM+XAttn	ID	ARKit	0.466 $\pm$ 0.192	0.612 $\pm$ 0.185
FM+XAttn	ID	MP3D	0.746 $\pm$ 0.169	0.842 $\pm$ 0.128
FM+XAttn	ID	ScanNet	0.675 $\pm$ 0.152	0.795 $\pm$ 0.118
FM+XAttn	ID	ZInD	0.808 $\pm$ 0.179	0.881 $\pm$ 0.135
FM+XAttn	OOD	ScanNet++	0.725 $\pm$ 0.144	0.832 $\pm$ 0.106
FM+XAttn	B	ScanNet++ RGB	0.729 $\pm$ 0.205	0.824 $\pm$ 0.166
U-Net	ID	3RScan	0.694 $\pm$ 0.260	0.787 $\pm$ 0.215
U-Net	ID	ARKit	0.567 $\pm$ 0.209	0.700 $\pm$ 0.184
U-Net	ID	MP3D	0.867 $\pm$ 0.157	0.919 $\pm$ 0.113
U-Net	ID	ScanNet	0.803 $\pm$ 0.160	0.880 $\pm$ 0.115
U-Net	ID	ZInD	0.885 $\pm$ 0.161	0.929 $\pm$ 0.119
U-Net	OOD	ScanNet++	0.870 $\pm$ 0.136	0.924 $\pm$ 0.094
U-Net	B	ScanNet++ RGB	0.761 $\pm$ 0.219	0.844 $\pm$ 0.170
PConv-UNet	ID	3RScan	0.694 $\pm$ 0.261	0.787 $\pm$ 0.215
PConv-UNet	ID	ARKit	0.560 $\pm$ 0.213	0.693 $\pm$ 0.187
PConv-UNet	ID	MP3D	0.862 $\pm$ 0.164	0.915 $\pm$ 0.117
PConv-UNet	ID	ScanNet	0.791 $\pm$ 0.171	0.872 $\pm$ 0.126
PConv-UNet	ID	ZInD	0.881 $\pm$ 0.165	0.926 $\pm$ 0.122
PConv-UNet	OOD	ScanNet++	0.870 $\pm$ 0.139	0.924 $\pm$ 0.097
PConv-UNet	B	ScanNet++ RGB	0.766 $\pm$ 0.218	0.847 $\pm$ 0.170

**Scene 1** (disconnected floor islands): U-Net leads at 0.975; FM+XAttn and Diffusion reach 0.824 and 0.821. **Scene 2** (coarse-shape drift): FM+XAttn recovers

**Table S7:** Per-dataset stochastic summary (mean $\pm$ std).

Method	Split	Dataset	ES	IoU <sub>m</sub>
LaMa-Ens.	ID	3RScan	0.243 $\pm$ 0.148	0.530 $\pm$ 0.270
LaMa-Ens.	ID	ARKit	0.308 $\pm$ 0.111	0.398 $\pm$ 0.182
LaMa-Ens.	ID	MP3D	0.132 $\pm$ 0.111	0.764 $\pm$ 0.179
LaMa-Ens.	ID	ScanNet	0.188 $\pm$ 0.102	0.660 $\pm$ 0.159
LaMa-Ens.	ID	ZInD	0.102 $\pm$ 0.116	0.831 $\pm$ 0.180
LaMa-Ens.	OOD	ScanNet++	0.149 $\pm$ 0.093	0.720 $\pm$ 0.155
Diffusion	ID	3RScan	0.215 $\pm$ 0.179	0.637 $\pm$ 0.276
Diffusion	ID	ARKit	0.306 $\pm$ 0.142	0.483 $\pm$ 0.211
Diffusion	ID	MP3D	0.107 $\pm$ 0.124	0.823 $\pm$ 0.160
Diffusion	ID	ScanNet	0.150 $\pm$ 0.125	0.763 $\pm$ 0.145
Diffusion	ID	ZInD	0.091 $\pm$ 0.121	0.849 $\pm$ 0.157
Diffusion	OOD	ScanNet++	0.097 $\pm$ 0.102	0.832 $\pm$ 0.124
Flow Match.	ID	3RScan	0.206 $\pm$ 0.161	0.640 $\pm$ 0.266
Flow Match.	ID	ARKit	0.298 $\pm$ 0.134	0.487 $\pm$ 0.206
Flow Match.	ID	MP3D	0.109 $\pm$ 0.123	0.824 $\pm$ 0.169
Flow Match.	ID	ScanNet	0.156 $\pm$ 0.125	0.757 $\pm$ 0.157
Flow Match.	ID	ZInD	0.094 $\pm$ 0.122	0.853 $\pm$ 0.167
Flow Match.	OOD	ScanNet++	0.101 $\pm$ 0.103	0.832 $\pm$ 0.135
FM+XAttn	ID	3RScan	0.194 $\pm$ 0.156	0.642 $\pm$ 0.256
FM+XAttn	ID	ARKit	0.275 $\pm$ 0.125	0.495 $\pm$ 0.193
FM+XAttn	ID	MP3D	0.101 $\pm$ 0.112	0.819 $\pm$ 0.154
FM+XAttn	ID	ScanNet	0.146 $\pm$ 0.116	0.748 $\pm$ 0.144
FM+XAttn	ID	ZInD	0.089 $\pm$ 0.115	0.855 $\pm$ 0.162
FM+XAttn	OOD	ScanNet++	0.095 $\pm$ 0.093	0.813 $\pm$ 0.123

best (0.913); Flow Matching and Diffusion trail at 0.801 and 0.788. **Scene 3** (residual boundary artifacts): U-Net achieves 0.996; Diffusion and FM+XAttn follow at 0.927 and 0.926.

#### S7.4 Structurally Challenging Subset

The astute reader may observe that All-Floor results in Tab. 3 perform as competitively as many models. Because ScanNet++ scenes are typically large open rooms with extensive floor coverage, the resulting observations have high floor prevalence on  $R_{\text{eval}}$  (mean  $r_{\text{cond}} \approx 0.89$ ), and the All Floor baseline achieves  $\text{IoU} \approx 0.854$ , nearly matching learned models. Such observations are dominated by label imbalance rather than model quality. To produce a meaningful comparison on canonical BEV inputs, we define a *structurally challenging* subset of the canonical test split, filtered by two criteria that jointly eliminate the label-dominance effect:

1. **Low conditioning signal:**  $r_{\text{cond}} \leq 0.20$  (Learnable tier, Sec. S2.5)—the model must predict  $\geq 80\%$  of the floor from  $\leq 20\%$  observed context.
2. **Low floor prevalence:** floor fraction on  $R_{\text{eval}} < 0.50$ —non-floor dominates the evaluation region, so predicting all-floor is no longer rewarded.

This yields  $N=1,386$  observations (mean  $r_{\text{cond}}=0.14$ , floor prevalence 0.19), substantially harder than standard evaluation. All predictions are drawn from the

**Table S8: Per-difficulty fidelity metrics** on the canonical test split ( $N=28,343$ ). *Easy*:  $r_{\text{cond}} > 0.20$  (most floor is observed); *Learnable*:  $0.10 \leq r_{\text{cond}} \leq 0.20$  (the model must infer  $\geq 80\%$  of the floor). ID = five training sources; OOD = ScanNet++. Bold = best per column.  $K$ -sample methods report the *best-of- $K=4$*  IoU.

Method	$K$	Easy-ID		Easy-OOD		Learn-ID		Learn-OOD	
		IoU $\uparrow$	F1 $\uparrow$						
All-Floor	1	0.785	0.846	0.859	0.916	0.563	0.647	0.833	0.894
NN Prop.	1	0.759	0.831	0.798	0.876	0.492	0.591	0.691	0.793
U-Net	1	<b>0.846</b>	<b>0.904</b>	0.877	0.929	<b>0.691</b>	<b>0.784</b>	<b>0.839</b>	<b>0.901</b>
PConv-UNet	1	0.843	0.902	<b>0.878</b>	<b>0.929</b>	0.680	0.775	0.836	0.898
LaMa	1	0.760	0.843	0.699	0.810	0.513	0.638	0.549	0.682
LaMa-Ens.	4	0.843	0.848	0.877	<b>0.915</b>	0.664	0.645	0.848	<b>0.893</b>
Diffusion	4	0.849	0.831	<b>0.890</b>	0.844	0.696	0.708	<b>0.861</b>	0.805
Flow Match.	4	<b>0.850</b>	<b>0.851</b>	0.887	0.874	0.684	0.691	0.833	0.807
FM+XAttn	4	0.849	0.843	0.879	0.840	<b>0.698</b>	<b>0.710</b>	0.836	0.796

Tier sizes: Easy-ID = 9,269, Easy-OOD = 13,293, Learn-ID = 2,860, Learn-OOD = 2,921.

**Table S9: Per-difficulty stochastic calibration** ( $K=4$ ). MES ( $\downarrow$ ): masked energy score; IoU $_b$  ( $\uparrow$ ): best-of- $K$  IoU; Var: mean per-pixel variance. Bold = best per column.

Method	Easy-ID			Easy-OOD			Learn-ID			Learn-OOD		
	MES $\downarrow$	IoU $_b\uparrow$	Var									
LaMa-Ens.	0.133	0.843	0.060	0.142	0.877	0.078	0.236	0.664	0.126	0.182	0.848	0.114
Diffusion	0.122	0.849	0.041	0.094	<b>0.890</b>	0.046	0.208	0.696	0.053	0.108	<b>0.861</b>	0.055
Flow Match.	0.121	<b>0.850</b>	0.032	0.096	0.887	0.038	0.213	0.684	0.052	0.121	0.833	0.063
FM+XAttn	<b>0.116</b>	0.849	0.040	<b>0.093</b>	0.879	0.058	<b>0.191</b>	<b>0.698</b>	0.055	<b>0.107</b>	0.836	0.074

existing canonical test-split cache (no new inference), ensuring identical model weights and protocol.

*Results.* Table S11 presents the hard-subset metrics. **All Floor collapses** to IoU=0.191 (UMR=0.809), confirming removal of the baseline advantage. Among deterministic methods, U-Net leads (IoU=0.468). Among stochastic best-of- $K=4$  methods, **FM+XAttn achieves the highest fidelity** (IoU=0.479) and **best calibration** (MES=0.316). This demonstrates that stochastic completion provides measurable gains on observations where the task is *genuinely hard*, *i.e.*, the model sees little floor, the unseen region is structurally complex, and trivial baselines fail.

## S8 Miscellaneous Notes

### S8.1 Scope of the Benchmark

*Excluded model families.* Autoregressive models require explicit spatial ordering and incur high latency on dense grids [28, 157]. Discrete-categorical diffusion adds transition-kernel complexity without clear gains on binary maps [1, 56]. Vector floorplan generators [87, 125] target global plan synthesis rather than conditional

**Table S10:** Sample-count sensitivity ( $K \in \{1, 2, 3, 4\}$ ) on both ID and OOD splits. All values are best-of- $K$  IoU ( $\uparrow$ ), which increases monotonically with  $K$  for every method and split. Bold marks the best  $K$  per method within each split.

Method	Split	$K=1$	$K=2$	$K=3$	$K=4$
LaMa-Ens.	ID	0.735 $\pm$ 0.304	0.787 $\pm$ 0.236	0.806 $\pm$ 0.214	<b>0.817 <math>\pm</math> 0.205</b>
LaMa-Ens.	OOD	0.853 $\pm$ 0.153	0.867 $\pm$ 0.130	0.871 $\pm$ 0.127	<b>0.874 <math>\pm</math> 0.126</b>
Diffusion	ID	0.699 $\pm$ 0.207	0.796 $\pm$ 0.220	0.819 $\pm$ 0.205	<b>0.830 <math>\pm</math> 0.196</b>
Diffusion	OOD	0.734 $\pm$ 0.148	0.866 $\pm$ 0.122	0.879 $\pm$ 0.123	<b>0.890 <math>\pm</math> 0.122</b>
Flow Match.	ID	0.722 $\pm$ 0.233	0.792 $\pm$ 0.223	0.817 $\pm$ 0.204	<b>0.829 <math>\pm</math> 0.192</b>
Flow Match.	OOD	0.771 $\pm$ 0.151	0.862 $\pm$ 0.127	0.874 $\pm$ 0.127	<b>0.880 <math>\pm</math> 0.129</b>
FM+XAttn	ID	0.716 $\pm$ 0.222	0.790 $\pm$ 0.214	0.818 $\pm$ 0.201	<b>0.830 <math>\pm</math> 0.192</b>
FM+XAttn	OOD	0.725 $\pm$ 0.144	0.842 $\pm$ 0.120	0.862 $\pm$ 0.121	<b>0.873 <math>\pm</math> 0.124</b>

**Table S11: Structurally challenging subset** (mean $\pm$ std,  $N=1,386$ ). UMR denotes *unobserved-region mismatch rate* (lower is better). Observations are filtered by  $r_{\text{cond}} \leq 0.20$  and floor prevalence  $< 0.50$  on  $R_{\text{eval}}$ , isolating cases where the model sees  $\leq 20\%$  of the floor and obstacles dominate the unseen region. All Floor collapses to IoU = 0.19 because predicting all-floor fails when non-floor dominates.  $K$ -sample methods report best-of- $K=4$ . Bold = best per column. **Right:** Stochastic calibration on the same subset.

Method	$K$	UMR $\downarrow$	IoU $\uparrow$	F1 $\uparrow$
All-Floor	1	0.809 $\pm$ 0.147	0.191 $\pm$ 0.168	0.302 $\pm$ 0.204
NN Prop.	1	0.337 $\pm$ 0.108	0.192 $\pm$ 0.153	0.299 $\pm$ 0.188
U-Net	1	<b>0.111 <math>\pm</math> 0.064</b>	0.468 $\pm$ 0.193	<b>0.609 <math>\pm</math> 0.164</b>
PConv-UNet	1	0.111 $\pm$ 0.066	0.458 $\pm$ 0.198	0.599 $\pm$ 0.170
LaMa	1	0.147 $\pm$ 0.079	0.317 $\pm$ 0.187	0.463 $\pm$ 0.188
LaMa-Ens.	4	0.790 $\pm$ 0.152	0.397 $\pm$ 0.231	0.296 $\pm$ 0.218
Diffusion	4	0.151 $\pm$ 0.081	0.462 $\pm$ 0.198	0.558 $\pm$ 0.178
Flow Match.	4	0.170 $\pm$ 0.087	0.464 $\pm$ 0.195	0.515 $\pm$ 0.185
FM+XAttn	4	0.155 $\pm$ 0.082	<b>0.479 <math>\pm</math> 0.191</b>	0.550 $\pm$ 0.175

Method	MES $\downarrow$	IoU $\uparrow$	IoU $_m$	Var
LaMa-Ens.	0.362 $\pm$ 0.158	0.397 $\pm$ 0.231	0.295 $\pm$ 0.216	0.174 $\pm$ 0.072
Diffusion	0.352 $\pm$ 0.153	0.462 $\pm$ 0.198	0.396 $\pm$ 0.202	0.055 $\pm$ 0.034
Flow Match.	0.346 $\pm$ 0.148	0.464 $\pm$ 0.195	0.394 $\pm$ 0.199	0.040 $\pm$ 0.028
FM+XAttn	<b>0.316 <math>\pm</math> 0.139</b>	<b>0.479 <math>\pm</math> 0.191</b>	<b>0.417 <math>\pm</math> 0.192</b>	0.046 $\pm$ 0.031

ID = 1,221, OOD = 165. Mean  $r_{\text{cond}}=0.14$ , mean floor prevalence = 0.19.

completion from a single observation with hard evidence clamping. We therefore restrict comparison to continuous stochastic families at matched capacity.

*Excluded datasets.* Several additional indoor corpora were evaluated but excluded. Novel-view-synthesis datasets (DL3DV-10K [74], RealEstate10K [164]) and depth benchmarks (NYUv2 [126], SUN RGB-D [128]) yielded sparse or metrically inconsistent floor reconstructions under both classical and modern multi-view fusion [89, 123, 148]. HM3DSem, the semantic subset of the HM3D dataset [111, 158], has per-room mesh annotations but lacks per-room mesh segments and requires a large overhead of processing meshes. SUN RGB-D [128] and SceneNN [58] add limited diversity for the additional storage overhead, but remain viable future options.

## S8.2 Implementation Details

*Hyperparameters.* All single-model runs use seed 42; LaMa-Ensemble uses seeds 41–44. Because the VGG perceptual loss and ResNet perceptual loss used in

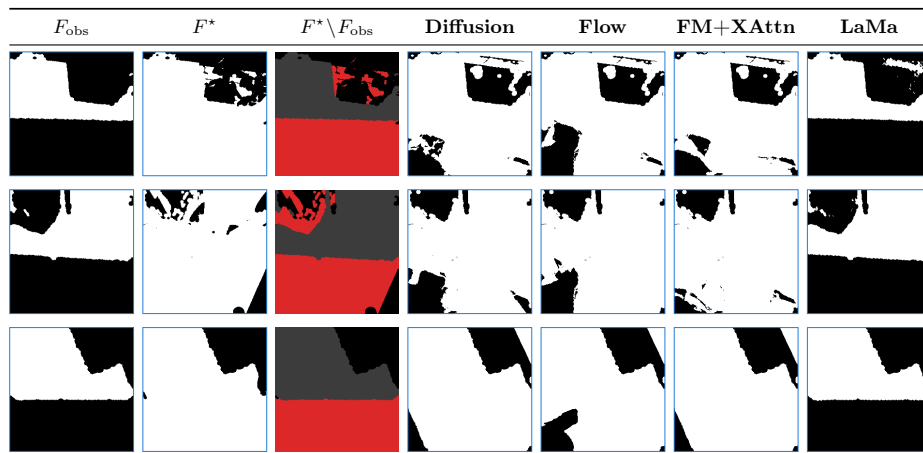


**Fig. S11: Supplementary failure cases.** Three additional test scenes exhibiting the failure patterns identified in Sec. 6: disconnected floor islands (row 1), coarse-shape drift (row 2), and residual boundary artifacts (row 3). The boundary-leakage case is shown in the main paper (Fig. 7). The red overlay ( $F^* \setminus F_{\text{obs}}$ ) shows GT floor absent from the observation (50–61% across cases). LaMa collapses in every case.

the original LaMa assume 3-channel natural-image inputs, both are disabled (weight=0); the remaining losses (masked  $\ell_1$  reconstruction, hinge adversarial loss, and multi-scale feature matching [60]) are channel-agnostic and retained unchanged (weights  $\lambda_{\text{rec}}=10$ ,  $\lambda_{\text{adv}}=10$ ,  $\lambda_{\text{fm}}=250$ ; see Tab. S12). Training runs on  $4 \times \text{A100}$  40 GB GPUs with distributed data-parallel, FP32, and activation checkpointing [26]; peak memory is 30–36 GB per GPU. At inference, we integrate the learned ODEs used in Flow Matching models from  $t=0$  to  $t=1$  using the second-order Heun solver [62]. We use DDIM [127] with 50 steps and classifier-free guidance (CFG) at scale  $s=2.0$  [53] for the diffusion model. CFG at scale  $s=2.0$  and per-step evidence clamping are applied for all models with dropout rate 0.1. All hyperparameters follow standard literature and implementations [53, 77, 145].

*Runtime and NFE summary.* Deterministic baselines require NFE=1; LaMa-Ensemble NFE=4 (one forward pass per seed). Diffusion and Flow Matching use 50 solver steps per sample, while FM+XAttn uses 25 solver steps per sample. This yields NFE=200 for Diffusion and Flow Matching ( $50 \times K$ ) and NFE=100 for FM+XAttn ( $25 \times K$ ). Deterministic models achieve  $>12$  FPS; stochastic generators are 20–80 $\times$  slower. FM+XAttn is the slowest despite fewer solver steps because cross-attention adds per-step overhead. We observed no significant difference in results at inference due to this change. All models were selected by peak validation micro-IoU; inference is fully deterministic given fixed noise seeds.

**Table S12: Training configuration and inference runtime. Top:** Hyperparameters shared across all learned models; LaMa-specific loss weights listed separately. **Bottom:** Per-observation latency and throughput on a single A100 (256×256 inputs).

Training hyperparameters				
Optimizer	AdamW [84]			
Learning rate	$1 \times 10^{-4}$			
Weight decay	$1 \times 10^{-2}$			
LR schedule	Cosine annealing [83] (no restarts)			
Effective batch size	64 (16/GPU × 4 GPUs)			
Training steps	300,000			
Precision	FP32			
Gradient accumulation [9]	1 step			
BCE positive weight	1.0 (floor and non-floor equally weighted)			
CFG dropout $p_{\text{drop}}$	0.1 (stochastic models only)			
LaMa / LaMa-Ensemble additional				
$\lambda_{\text{rec}} / \lambda_{\text{adv}} / \lambda_{\text{fm}}$	10.0 / 10.0 / 250.0			
Seeds (LaMa-Ensemble)	41, 42, 43, 44			
Inference runtime				
Method	Sampler	NFE	Latency (ms)	FPS
U-Net	Forward	1	81	12.3
PConv-UNet	Forward	1	68	<b>14.7</b>
LaMa	Forward	1	<b>63</b>	<b>15.9</b>
LaMa-Ens.	Forward	4	136	7.4
Diffusion	DDIM	200	1745	0.6
Flow Match.	Heun	200	3377	0.3
FM+XAttn	Heun	100	6661	0.2

## S9 Ethical Considerations

*Ethical use.* This work targets assistive robotics, accessibility mapping, and autonomous indoor navigation. The binary BEV representation abstracts away visual appearance, so the model neither processes nor generates identifiable imagery. Inferring layout beyond the visible region could facilitate unauthorized mapping of private spaces. We recommend red-teaming, access-control policies, and audit logging at deployment.

*Privacy and data provenance.* All six source datasets were collected with informed consent under their respective institutional review processes. Researchers must obtain source data under the original licenses [7, 24, 34, 36, 147, 160]. The derived BEV maps contain no personally identifiable information.

*Dataset Bias and environmental impact.* The source corpora are predominantly North American and European interiors; models may under-perform on under-represented building typologies. Training the seven learned models required approximately 280 A100-GPU hours on a shared institutional cluster powered in part by renewable energy; per-model runtime is reported in Tab. S12.